



HAL
open science

Intermediate filaments promote glioblastoma cell invasion by controlling cell deformability and mechanosensitive gene expression

Emma J van Bodegraven, David Pereira, Florent Peglion, Elvira Infante, Yekta Kesenci, Emmanuel Terriac, Juliana Geay, Vanessa Roca, Marina Plays, Laura Soto, et al.

► To cite this version:

Emma J van Bodegraven, David Pereira, Florent Peglion, Elvira Infante, Yekta Kesenci, et al.. Intermediate filaments promote glioblastoma cell invasion by controlling cell deformability and mechanosensitive gene expression. 2023. pasteur-04257830

HAL Id: pasteur-04257830

<https://pasteur.hal.science/pasteur-04257830v1>

Preprint submitted on 25 Oct 2023

HAL is a multi-disciplinary open access archive for the deposit and dissemination of scientific research documents, whether they are published or not. The documents may come from teaching and research institutions in France or abroad, or from public or private research centers.

L'archive ouverte pluridisciplinaire **HAL**, est destinée au dépôt et à la diffusion de documents scientifiques de niveau recherche, publiés ou non, émanant des établissements d'enseignement et de recherche français ou étrangers, des laboratoires publics ou privés.



Distributed under a Creative Commons Attribution 4.0 International License

Intermediate filaments promote glioblastoma cell invasion by controlling cell deformability and mechanosensitive gene expression

Sandrine Etienne-Manneville (✉ sandrine.etienne-manneville@pasteur.fr)

CNRS-Institut Pasteur <https://orcid.org/0000-0001-6651-3675>

Article

Keywords:

Posted Date: June 29th, 2023

DOI: <https://doi.org/10.21203/rs.3.rs-2828066/v1>

License:   This work is licensed under a Creative Commons Attribution 4.0 International License.

[Read Full License](#)

Additional Declarations: There is **NO** Competing Interest.

Cytoplasmic intermediate filaments promote glioblastoma cell invasion by controlling cell deformability and mechanosensitive gene expression

Emma J. van Bodegraven^{1,5}, David Pereira^{2,3*}, Florent Peglion^{1*}, Elvira Infante^{1*}, Yekta Kesenci^{4*}, Emmanuel Terriac¹, Juliana Geay^{1,6}, Vanessa Roca¹, Marina Plays¹, Laura Soto¹, Shailaja Seetharaman^{1,7}, Batiste Boëda¹, Jean-Christophe Olivo-Marin⁴, Atef Asnacios³, Aleix Boquet-Pujadas^{4,8}, Jean-Baptiste Manneville^{2,3}, Sandrine Etienne-Manneville¹

¹ Cell Polarity, Migration and Cancer Unit, Institut Pasteur, Université de Paris, Equipe Labellisée Ligue 2023, F-75015, Paris, France.

² Institut Curie, PSL Research University, CNRS, UMR 144, 26 rue d'Ulm F-75005, Paris, France

³ Laboratoire Matières et Systèmes Complexes, UMR 7057, CNRS and Université de Paris Cité, CNRS, UMR7057, 10 rue Alice Domon et Léonie Duquet, F-75013,75205 Paris cedex 13, France

⁴ Bioimage Analysis Unit, Institut Pasteur, UMR3691 CNRS, Université Paris Cité, Paris, France.

⁵ current address: Department of Translational Neuroscience, UMC Utrecht Brain Center, University Medical Center Utrecht, Utrecht University, 3584 CG, Utrecht, The Netherlands

⁶ current address: CytoMorpho Lab, CEA, Université de Paris, IPGG, Paris, France

⁷ current address: James Franck Institute, Department of Physics, University of Chicago, USA

⁸ current address: Biomedical Imaging Group, École polytechnique fédérale de Lausanne, Lausanne, Switzerland

*equal contribution

Correspondence to Sandrine Etienne-Manneville, setienne@pasteur.fr

Abstract

Cancer invasion turns a locally growing tumour into a live-threatening disease. Unravelling the molecular signature of invasive cells and their mechanisms of invasion is essential to identify therapeutic targets. While the cytoskeleton is known to support cell mechanical properties required for invasion, the role of intermediate filaments (IFs) is often overlooked. Here we investigated the role of IFs in glioblastoma (GBM), the most common and aggressive primary brain tumour, which is characterized by its high invasive capacity, allowing it to evade classical treatments. Following in silico analysis of published single cell RNA sequencing data of GBM samples which shows that high expression of IF genes correlates with pro-migration markers, we generated IF-depleted GBM cells to demonstrate that the cytoplasmic IF network promotes GBM cell invasion in vitro and in vivo. Mechanical measurement and biochemical analyses show that IFs influence cell invasion by increasing cell stiffness, limiting nuclear deformations, and controlling mechanosensitive gene expression and matrix degradation. Our results reveal the crucial role of IFs in tumour cell mechanics and invasion and suggest that the IF expression pattern can serve as a molecular marker of cells driving glioblastoma invasion.

Introduction

Cell invasion is a process that involves the migration of cells through complex and changing 3D microenvironments. It is essential during development, for immune responses or tissue remodelling in the adult, and is associated with pathological situations. Cancer invasion is a landmark event that transforms a locally growing tumour into a systemic, metastatic, and life-threatening disease. Glioblastomas (GBM), which originate from glial cells, glia precursors or neural stem cells, are the most common malignant primary brain tumours. This type of cancer is rare but devastating as there is no curative treatment available. The invasive character of GBM is one of the main contributors to the poor prognosis for patients as cells migrate away from the tumour core, evade therapy and initiate recurrence. Tumour invasion was recently shown to be the main cause of death in GBM patients ¹. GBMs are also very heterogeneous ² and the migratory behaviour of GBM differs across patients, and even within the same tumour different migratory behaviours are observed ³. There is an urgent need for a molecular signature of the invasive properties of GBM and for new therapeutic targets. However, the molecular alterations responsible for GBM cell invasion are still obscure.

From a physical point of view, cell invasion relies on the generation of forces to move through complex 3D environments and, at the same time, on appropriate mechanical features to allow cell deformation without damage. Cell invasion thus depends on the intrinsic mechanics of the cells. In principle, it is easier for an overall-softener, more deformable cell to migrate through small gaps, crowded matrices or entangled matrix fibres, leading to the hypothesis that the deformability of individual cells correlates with their invasive potential ⁴. Several *in vitro* experiments and animal studies also indicate that the mechanical properties of the environment significantly contribute to GBM invasion ⁵⁻⁸. Mechanosensing allows cells to sense the mechanical properties of the microenvironment. In response to these cues, mechanotransduction leads to the generation of intracellular biochemical signals that influence gene transcription and cytoskeletal organization. Studies on patient tissues and xenograft models suggest that GBM aggressiveness is linked with tissue stiffness, stiffness related changes in the extracellular matrix, and increased levels of markers that indicate mechanosensing and mechanotransduction ⁹. Identifying the cellular elements involved in both the intrinsic mechanical properties of cells and mechanotransduction is necessary to better understand how invading cells adapt their mechanical properties to their environment, and how oncogenic changes can influence tumour cells to invade surrounding tissues.

Cell mechanical properties and cell invasion heavily rely on the cytoskeleton, which is mainly composed of actin, microtubules and intermediate filaments (IFs). IFs are ten nanometers in diameter

and are formed by self-assembly of core proteins, which are much more diverse than the globular actin and tubulin families ¹⁰. Changes in IF composition are associated with tumour invasion and poor prognosis ¹¹. The best-known examples are vimentin IFs, which form a major cytoskeletal component of motile mesenchymal cells and metastatic tumours of epithelial origin. Vimentin is overexpressed during epithelial to mesenchymal transition and promotes cell migration and invasion ^{12,13}. In GBM, changes in IF composition have been associated with tumour invasion and aggressiveness as well ^{14,15}. We and others have shown that IFs control acto-myosin contractility via a Rho-mediated signalling pathway during 2D cell migration, suggesting that they may be instrumental during mechanotransduction ^{16,17}. Moreover, the composition and structure of IFs results in unique mechanical properties which have an impact on cell deformability ¹⁸⁻²¹. This led us to investigate the expression of IFs in GBM cells and their contribution to GBM cell invasion.

Here, we first analyse published single-cell RNA-sequencing data and find that, within tumours, cell heterogeneity is reflected in a large variety of expression patterns of cytoplasmic IF proteins and show that IF expression correlates with invasive property markers in GBM patients. Comparison of IF-expressing and IF-depleted GBM cells demonstrates the crucial role of IFs in cell invasion both *in vitro* and *in vivo*. In this context, by combining single cell mechanical characterization and biochemical signalling analysis, we could reveal the specific functions of IFs in the control of cell mechanical properties, in mechanical shielding of the nucleus, mechanosensitive signalling, and gene expression needed for ECM degradation during cell invasion.

Results

IF gene expression correlates with a pro-migratory signature in patient GBM cells

To identify IF expression patterns in GBM, we analyzed published single-cell RNA sequencing (scRNAseq) patient data from eight isocitrate dehydrogenase wild-type (IDHwt) GBM ²² (Figure 1A). Neoplastic cell populations were identified for each patient (Supplementary Figure 1A, 1B) and integrated to identify common neoplastic cell populations (Supplementary Figure 2A). 15 different neoplastic cell populations were identified in which the IF genes vimentin (*VIM*), glial fibrillary acidic protein (*GFAP*), nestin (*NES*), and synemin (*SYNM*) are heterogeneously expressed (Supplementary Figure 2A, 2B). Cells were grouped based on the expression of *GFAP*, *VIM*, *NES*, and *SYNM* in a hierarchical cluster analysis (Supplementary Figure 2C). Filtering of these cell clusters revealed 12 different IF expression patterns in IDHwt GBM (Figure 1B) with a wide range of total IF expression levels and a large group of cells (30%) without any detectable cytoplasmic IF mRNA (Supplementary Figure 2D, 2E)(Supplementary Table 1). All IF expression patterns were found in neoplastic cells of

multiple patients at varying levels (Supplementary Figure 2D), illustrating the intra- and intertumoral heterogeneity of IFs in GBMs.

To explore the cellular functions related to IF expression levels and specific patterns, differential gene-expression analysis was performed between cells with different IF expression patterns (IF cell clusters) (Supplementary Table 2) followed by a Gene Ontology analysis (Supplementary Table 3). We found 'positive regulation of cell migration', 'extracellular matrix reorganization' and 'angiogenesis' as recurring GO clusters associated with high expression of IF genes, while genes belonging to the GO cluster of 'cell division' were associated with low IF gene expression levels (Figure 1C and Supplementary Figure 2F-I). These results indicated an overall correlation of total IF gene expression to a migration-related gene signature. We then used a larger recently published resource of GBM single cell RNA sequencing data in which 16 different datasets of 99 GBM grade IV patients in total were integrated²³ to determine whether the presence of IFs was associated with the pro-migratory genes (Figure 1D)(Supplementary Figure 2J). We selected GBM cells with an IF gene signature predicted to result in filament formation in cells ('filaments') (cells expressing at least *VIM* or *GFAP*). Cells expressing only *SYNM* or *NES* which cannot form filaments on their own^{24,25}, were combined with IF 'negative' cells into a 'no filaments' IF gene signature group. Module scores of migration-related genes, periphery markers²⁶, and GBM invasion-related genes (Yu et al., 2020) were significantly higher in cells with a 'filaments' IF gene expression signature compared to 'no filaments' (Figure 1E-G), whereas module scores for cell division-related genes showed a trend for a decrease in 'filaments' cells (Supplementary Figure 2K). Out of the four IF genes, *VIM* positive cells showed the strongest association with a migration- and invasion-related gene signature (Figure 1H, 1I). Altogether our analysis shows a clear correlation between the presence of cytoplasmic IFs and migration- and invasion-related gene-expression signatures in GBM patients and suggest that high levels of vimentin-containing IFs characterize the most invasive cells.

The IF network is essential for glioblastoma cell invasion

To determine whether vimentin IFs were required for GBM cell migration and invasion, we used CRISPR/Cas9 to knockout vimentin in U251 GBM cells. We obtained a heterogeneous population of cells with a strong down regulation of vimentin mRNA (Supplementary Figure 3A), without any detectable vimentin protein and vimentin filaments (Figure 2A-C). This population also showed a strong inhibition of *GFAP*, *nestin* and *synemin* mRNA (Supplementary Figure 3A) and protein expression (Figure 2B). Overall, the vimentin KO strategy resulted in the absence of any cytoplasmic IF network (Figure 2C, 2D) allowing us to test the contribution of the IF network to GBM invasion. From here on we use the term 'IF-depleted cells' for this mixed population of vimentin knockout cells which do not have any cytoplasmic IFs.

We first assessed the invasive capacity of control and IF-depleted GBM cells following injection in the zebrafish brain ²⁸ (Figure 2E). Fluorescently-labelled cells, injected in the optic tectum of Tg(*gfap:gfp*) zebrafish invaded into the brain parenchyma in 3D (Figure 2F). 72h after injection, the invasion index (defined as the ratio between the 3D invaded area and the initial area occupied by GBM cells) of IF-depleted cells was much lower (more than 60% less) than that of control cells (Figure 2G, 2H), demonstrating that IFs are essential for GBM cell invasion *in vivo*.

To determine whether the altered invasion of IF-depleted cells *in vivo* was due to a decrease in intrinsic cell invasive properties or cell non-autonomous effect, we further analysed GBM cell invasion in an *in vitro*, 3D extracellular matrix (ECM). GBM cells were grown as spheroids, embedded in Matrigel, and followed by live-cell imaging (Figure 2I; Supplementary Video 1). Control and IF-depleted cells formed initial spheres of similar size (Supplementary Figure 3B). While the size of the spheroids core after 40 hours of invasion was not different (Supplementary Figure 3C), IF depletion strongly decreased cell invasion in the Matrigel (Supplementary Figure 3D, 3E). The number of cells separating from the IF-depleted spheroids ('invading cells') was dramatically reduced compared to control spheroids (Figure 2J), demonstrating that IFs play a direct role in the intrinsic invasive properties of GBM cells.

During invasion GBM cells tend to form chains (Supplementary Video 2) in which, leader cells have been shown to drive invasion of followers and display specific molecular properties ²⁹. In IF-depleted cells both leaders and followers were strongly reduced (Figure 2K). We then generated mixed spheres with an equal number of control and IF-depleted cells. After 40h, control cells represented about 75% of leader cells, illustrating a strong alteration in the formation of leaders by IF-depleted cells (Figure 2L, 2M). Interestingly, this difference was reduced amongst followers, which included 60% of control cells and 40% of IF-depleted cells (Figure 2M). Interestingly, addition of control IF-expressing cells to IF-depleted cells led to an increase in the number of IF-depleted followers (Figure 2N), suggesting that IF-expressing cells can lead and thereby promote the invasion of IF-depleted cells. Overall our data demonstrate that the IF network strongly promotes cell invasion both *in vitro* and *in vivo* and highlights the crucial role of IFs in promoting leader cells.

The IF network reduces cell deformability and the ability to migrate through tight spaces

In vitro and *in vivo*, the ability of cells to move and squeeze through dense environments largely depends on their mechanics. Since IFs are known to influence the mechanics of various cell types ¹⁸, we first compared the mechanical properties of control and IF-depleted cells using a single cell microplate rheometer ³⁰. Cells were subjected to oscillatory uniaxial compressions with an amplitude of ~1 μm (Figure 3A). IF-depleted cells showed a 40% decrease in the shear modulus (G) with both a decrease in the elastic storage modulus (G') and viscous loss modulus (G'') (Figure 3B), suggesting that

cortical stiffness is reduced in IF-depleted GBM cells³¹. We then used an intracellular microrheology method to more precisely describe the intracellular viscoelastic properties³². Internalized beads (2 μm diameter) were optically trapped and the cell was displaced in a stepwise fashion (Figure 3C). Viscoelastic relaxation curves showed a faster relaxation of the bead displacement in IF-depleted cells (Figure 3D). The initial bead step displacement (X_b) and rigidity index which both positively correlate with the rigidity of the cytoplasm were significantly reduced in IF-depleted cells (Figure 3E, 3F). Fitting the relaxation curve with the standard linear liquid viscoelastic model yields the spring constant K and the dynamic viscosity η . The spring constant K (Figure 3G), but not the viscosity η (Figure 3H), was significantly reduced for IF-depleted cells. Altogether these results strongly suggest that IF-depleted cells are more deformable than control, IF-expressing cells.

The impact of IF expression on cell deformability may influence GBM cell invasion through the dense environment. To assess their migration in a confined, geometrically-controlled environment, we used fibronectin-coated PDMS microchannels of 5 μm x 6.5 μm (Figure 3I). GBM cells fluorescently labelled with a cytoplasmic and DNA probe migrated at a similar speed (Figure 3J). We then generated 10 μm -wide microchannels with constrictions to further assess the cells' ability to squeeze through 1.5 μm -, 2 μm -, and 5 μm -wide spaces (Figure 3K, Supplementary Video 3). The 5 μm -wide constrictions rarely blocked cell migration ($\sim 90\%$ of cells passed through the constriction) and did not elicit any difference between control and IF-depleted cells (Figure 3L, 3M). In contrast, the 1.5 μm - and 2 μm -wide constrictions blocked the passage of a significant number of cells. The percentage of blocked cells was significantly higher in control cells than in IF-depleted cells (Figure 3L, Supplementary Video 3). Moreover, when going through the 2 μm -wide constriction, the transit time of control cells was on average more than 2.5 hours longer than that of IF-depleted cells (Figure 3M). These results show that IFs decrease cell deformability and cell's ability to migrate through narrow constrictions, but do not explain why IF-expressing cells are more invasive than IF-depleted cells.

The IF network promotes glioblastoma invasion via the expression of matrix metalloproteases

Cell invasion in a 3D ECM *in vitro* or *in vivo* relies on cell deformation through small spaces, but also on active degradation and remodelling of the surrounding ECM. Interestingly, our analysis of patient data showed a strong association between IF gene expression and expression of genes involved in ECM remodelling (Figure 1C, Supplementary Figure 2G). Matrix metalloproteinases are the main family of proteins able to degrade the ECM during cell invasion. Therefore, we tested whether matrix metalloproteinase (MMP) activity was required for control and IF-depleted cell invasion in 3D hydrogels. Treatment with the general MMP inhibitor GM6001 strongly reduced the invasion of control cells to a level similar to that of untreated IF-depleted cells, without significantly affecting the

invasion of IF-depleted cell (Figure 4A, 4B). These observations suggest that MMP activity plays a major role in the invasive properties of IF-expressing cells.

To test this hypothesis, GBM spheroids were embedded in 3D collagen gels in order to detect collagen degradation (^{3/4}Col1) (Figure 4C). Quantification of collagen degradation showed that control cells have a higher collagenase activity than IF-depleted cells (Figure 4D). Furthermore, analysis of MMP expression in patient-derived single-cell data showed that out of all detected MMPs in GBM cells, expression of MMP14 showed the strongest difference between cells with a 'no filament' and 'filament' IF gene expression signature (Figure 4E-G). The role of IFs in the expression of MMP14 was confirmed by comparing MMP14 mRNA and protein levels in control and IF-depleted GBM cells (Figure 4H-I). Moreover, depletion of MMP14 by shRNA (Figure 4J) led to a dramatic decrease in control cell invasion into the 3D Matrigel and totally abolished the difference of invasion between control and IF-depleted cells (Figure 4K). Altogether, these results demonstrate that IF expression promotes MMP14 expression and matrix degradation. They strongly suggest that the remodelling of the ECM is the main cause of the increased invasion of IF-expressing GBM cells.

The IF network forms a perinuclear cage which protects the nucleus from mechanical stress

We then investigated how cytoplasmic IFs may influence MMP14 transcription and matrix degradation. Cell migration in a confined environment suggested that IFs may impair the cell's ability to squeeze its nucleus during cell migration through tight constrictions (Figure 3L, 3M), leading us to assess the impact of cytoplasmic IFs on nuclear responses to mechanical stress. Using a single cell microplate rheometer, cells were squeezed from their original size in suspension (~10-15µm) to a thickness of 3 µm, smaller than the size of the nucleus (Figure 5A). Both the maximum force and stress needed to induce this large deformation were lower for IF-depleted cells compared to control cells (Figure 5B, 5C). Intracellular rheology using optical tweezers to probe the nucleus showed that the role of cytoplasmic IFs was not due to an indirect effect on the nuclear mechanical properties (Supplementary Figure 4A-F), suggesting that IFs may act as a physical barrier limiting the transmission of external compressive forces through the cytoplasm onto the nucleus.

The IF network concentrates around the nucleus to form a perinuclear cage in GBM cells plated on adhesive micropatterns (Figure 5D), moving through small constrictions (Figure 5E), or invading in a hydrogel (Matrigel) (Figure 5F), as observed in other cell types^{33,34}. To determine the specific role of this perinuclear cage in the transmission of forces to the nucleus, we used optical tweezers to oscillate beads located in the cytoplasm a few micrometers away from the nucleus (Figure 5G). The bead displacement induced a deformation of the nucleus edge facing the bead (Figure 5G-I) showing that forces are transmitted from the cytoplasm to the nucleus. In IF-depleted cells, the amplitude of the

bead oscillations was larger than in control cells (Figure 5J, 5K), confirming that these cells have a softer cytoplasm (Figure 3C-H). As a proxy for force transmission from the cytoplasm to the nucleus, we used the ratio between the nucleus deformation and the bead amplitude and found a higher ratio in IF-depleted cells (Figure 5L). Our results suggest that the IF nuclear cage buffers the transmission of mechanical stresses to the nucleus.

IFs limit mechanosensitive nuclear responses during cell invasion

We then analysed nuclear deformations in control and IF-depleted cells during invasion. When control and IF-depleted GBM cells invaded the zebrafish brain (Tg(fli1a:gfp)), IF-depleted cells extended protrusions along blood vessels similar to control cells, but the cell body remained almost immobile and frequently displayed very large deformations (Figure 6A, 6B, Supplementary Video 4). To quantify nuclear deformations, GBM spheroids formed of cells labelled with a fluorescent DNA probe were embedded in Matrigel and imaged in 3D using spinning-disk microscopy (Figure 6C). Fast acquisitions were used to analyse the nuclear deformations in 3D (Supplementary Video 5). IF-depleted leader cells showed more nuclear deformations than control leader cells, whereas there was no significant difference between follower cells (Figure 6D) suggesting that cytoplasmic IFs play a predominant role in protecting the nucleus from the compressive forces exerted on leader cells.

Nuclear deformations have been shown to influence the translocation of the transcription factors, such as YAP³⁵. In agreement with the measurements of nuclear deformations the nuclear YAP translocation (nuclear/cytoplasmic mean grey value) was significantly increased in IF-depleted leader cells compared to control leader cells. In contrast, no significant difference was observed between control and IF-depleted follower cells (Figure 6E, 6F). Altogether our observations show that IFs limit nuclear deformation more specifically in leader cells, in line with the specific impairment of IF-depleted cells to serve as leaders (Figure 2M, 2N) and also strongly suggest a role of IFs in controlling mechanosensitive gene expression³⁶.

Our observations prompted us to explore whether increasing compressive forces could affect metalloproteinase activity. Control and IF-depleted spheroids were embedded in a 3D collagen hydrogel. We then added high molecular weight dextran to the medium causing water to diffuse out of the hydrogel because of osmotic pressure, and indirectly leading to the mechanical compression of embedded cells³⁷. This mechanical compression reduced collagen degradation by invading control cells, demonstrating the mechanosensitivity of collagen degradation. In contrast, compression had no effect on IF-depleted cells (Figure 6G, 6H), whose ability to degrade collagen was already very low prior the addition of dextran. Altogether our results show that the cytoplasmic IF network buffers mechanical stresses applied to the nucleus, thereby participates in mechanotransduction under compressive forces, mechanosensitive matrix degradation and cell invasion.

Discussion

Our study highlights a causal link between IF protein expression and tumour cell invasion. We first show a correlation between IFs and pro-migratory pathways in patient samples and then demonstrate that the IF network plays a crucial role in GBM cell invasion both *in vitro* and *in vivo*. Our results highlight several connected mechanical functions of IFs during cell invasion. Cytoplasmic IFs contribute to cell rigidity by modulating both the cytoplasmic and the cortical mechanics of the cells. Thus, IF expression reduces cell deformability which is likely to prevent cell invasion through environments with a small mesh size. At the same time, cytoplasmic IFs form a perinuclear cage which protects the nucleus from deformation under compressive forces and reduces the transmission of forces to the nucleus. In the case of GBM cell invasion in 3D Matrigel or in brain tissues, cellular rigidity and the protective nuclear cage provided by the IF network lead to an increase in cell invasion mainly due to the effect of IFs on the mechanosensitive degradation of the extracellular matrix.

GBM invasion relies on the ability of GBM cells to migrate through brain tissue. GBM cells generally migrate in a mesenchymal manner as single cells³⁸ or as collectives³⁹. Mesenchymal cell invasion generally relies on the acto-myosin network, but microtubules have also been involved in endothelial and GBM cell invasion^{28,40}. However, the role of IFs, another major cytoplasmic cytoskeletal network, in cell invasion was not known. Here we show that IFs play an essential, yet versatile role in cell invasion.

Both *in vivo* and *in vitro*, IF-depleted cells generated protrusions similar to that of control cells, indicating that IFs are not necessary to push the membrane forward (Figure 6M). Mesenchymal migration also requires the generation of traction forces exerted on the ECM via focal adhesions. We previously showed in primary astrocytes that IFs restrict acto-myosin contractility and traction forces to leader cells to promote collective 2D sheet-like migration¹⁶. In GBM cells, loss of IFs also increased acto-myosin cables (Supplementary Figure 5A-B). However, GBM cells do not migrate as collective monolayers in 2D and the effect of IF depletion in 2D random migration was limited (Supplementary Figure 5C, 5D). Once in a confined environment, control and IF-depleted cells migrated at the same speed (Figure 3J). It is only in *in vitro* and *in vivo* environments that IFs strongly promote migration, suggesting that they contribute to the ability of the cell to squeeze through tight spaces or to remodel their environment. In our study, control and IF-depleted cells display similar cellular and nuclear sizes (Supplementary Figure 5E-G). The absence of IFs increases cell deformability both at the cortical and the cytoplasmic levels as has been observed previously, depending on the cellular context and experimental approach^{17,18}. In GBM cells, loss of IFs mainly resulted in a decrease in cytoplasmic elasticity, while a slight reduction in viscosity was also observed but was not statistically significant. When the whole cell was probed, both elasticity and viscosity were decreased in IF-depleted cells,

probably reflecting the impact of the IF network on the cell cortex and the contribution of other cytoskeletal components¹⁷. When cells go through narrow constrictions in microchannels, the nucleus which is the stiffest cell organelle, is also strongly deformed. Although the loss of IFs does not alter the overall rigidity of the nucleus (Supplementary Figure 4A-F), we show that less force is required to squeeze the nucleus to 3 μm (Figure 5A-C). The mechanical protection together with the steric hindrance caused by the IF perinuclear cage are most likely responsible for the impaired migration of control cells through tight constrictions.

In the human brain and in the 3D Matrigel used in this study, pores can be smaller than 1 μm in diameter⁴¹. In these conditions, control GBM cells can barely move by deformation only, and require MMP activity, and in particular MMP14 expression, to invade 3D Matrigel (Figures 4). In contrast, cells devoid of cytoplasmic IFs show very limited metalloproteinase activity *in vitro* (Figure 4C, 4D) as well as in patients (Figure 4E-G). Their increased deformability does not allow them to invade as efficiently as control cells, and in the zebrafish brain, IF-depleted cells appeared more deformed but yet unable to move forward (Figure 6A, 6B, and Supplementary Video 4). Our results indicate that in 3D Matrigel and in the brain tissue of the zebrafish, MMP activity, but not cell deformability, is the factor promoting cell invasion. However, it is tempting to speculate that the relative roles of MMP activity and of cell deformability vary depending on the combined biochemical and mechanical properties of the surrounding environment.

The control of gene expression by cytoplasmic IFs can involve several molecular mechanisms including a direct regulation of signalling pathways controlling transcription factors⁴². Here however, we found that collagenase activity is inhibited by compressive forces, suggesting that mechanotransduction is involved in the regulation of MMP expression. As previously shown, large deformations during confined migration can globally shut down gene transcription through epigenetic modifications of the genome⁴³. This mechanism could be at the basis of the reduction in MMP14 expression, matrix degradation, and invasion of the more deformable IF-depleted cells. Alternatively, more subtle mechanosensitive pathways regulating the nuclear translocation of transcription factors may be at play. Interestingly, while nuclear YAP increased with substrate stiffness in sparse cells plated on substrates of different rigidities as reported previously⁴⁴, we did not observe any difference in nuclear translocation of YAP between control and IF-depleted cells (Supplementary Figure 5H, 5I), suggesting that IF-depletion does not impact integrin-mediated mechanosensing, but influences YAP translocation to the nucleus by facilitating nuclear deformations in 3D. It was shown recently that the opening of nuclear pores upon compression of the nucleus allows the entry of proteins such as YAP⁴⁵. A large variety of mechanosensitive transcription factors may thus be affected by the function of IFs as a mechanical buffer to nuclear deformations.

Overall, our study demonstrates the dual contribution of cell intrinsic mechanical properties to cell deformability as well as to mechanosensitive regulation of nuclear functions. These two aspects play critical and possibly opposite roles during cell invasion. The analysis of patient-derived scRNAseq data, which showed an association between IF gene expression and a migration- and invasion-related gene signature, also highlights the heterogeneous expression of IFs within the same tumour. Each IF protein participates through its unique head and tail domains in specific molecular interactions, which can differently modulate the mechanical properties of the IF network, of the cytoskeleton and eventually of the cell. The relative level of expression of GFAP splice variants which only differ in 42 amino acids in their tail domains already influence GBM cell invasive paths^{14,15,46}. Interestingly, we noticed that in patient-derived data, the expression of invasion- and migration-related genes is particularly high in cells expressing *SYNM* in combination with other IFs (Supplementary Figure 2F-H). Therefore, future studies focusing on individual IF proteins or different IF network compositions could reveal IF protein-specific functions. More generally, our observations suggest that a limited number of GBM cells with an extended IF network can form leader cells that will then facilitate the invasion of other possibly IF-negative cells to drive tumour spreading. The analysis of patient-derived data highlights that a large population of cells without detectable expression of IFs or expression of single IFs which cannot polymerize into a network (*SYNM* and *NES*) is present in almost all tumours, suggesting that high levels of IF expression may serve as a molecular marker of potential leader cells and consequently of the invasive potential of a given tumor. It also suggests that targeting the IF network of GBM cells could provide a novel strategy in the development of new complementary therapies to improve GBM treatment.

Online Material and methods

Single cell RNA sequencing analysis

Identification of neoplastic cells

Single cell RNA sequencing data from four grade IV IDHwt GBM patients obtained by Yuan et al., (2018) with a total of 12464 cells and four grade IV IDHwt GBM patients obtained by Darmanis et al., (2017) with a total of 3589 cells was used for the analysis. Raw read counts of cells which passed the quality control performed by the authors were downloaded and used for the analysis. For each individual patient, the Uniform Manifold Approximation and Projection (UMAP) non-linear dimension reduction analysis was performed to identify different cell populations using Seurat version 4.1.3. Markers of the different cell populations were identified by differential gene expression analysis between the clusters (FindAllMarkers function). Based on these cluster markers, cell clusters were manually scored as neoplastic or non-neoplastic (astrocytes, neurons, oligodendrocytes, microglia, endothelial cells). Neoplastic and non-neoplastic identity of cells was confirmed by a scRNAseq-derived copy number variation (CNV) analysis described previously⁴⁷. In short, the average of Seurat normalized read counts of all genes on each somatic chromosome was calculated for each neoplastic cell. These values were normalized to the average expression of all genes on each somatic chromosome of all of the non-neoplastic cells. This method has been confirmed to correspond to whole genome sequencing CNV analysis⁴⁷. Heatmaps were computed to visualize scRNAseq derived CNV values per neoplastic cell per patient (ggplot2 version 3.4.0). Amplification of chromosome 7 and/or deletion of chromosome 9 and 10 across neoplastic cells were used to confirm neoplastic cell identity (Supplementary Figure 1). Populations were removed when cell clusters deviated from the scRNAseq derived CNV values of other neoplastic cells within the same patient. This resulted in transcriptomic data from 489 neoplastic cells derived from patient 1, 1169 from patient 2, 1524 from patient 3, 389 from patient 4, 1261 from patient 5, 2197 from patient 6, 5924 from patient 7, 3084 from patient 8.

Integration of scRNAseq data and identification of neoplastic cell clusters

Datasets were integrated on the Seurat version 4.1.3 (FindIntegrationAnchors function) . The UMAP non-linear dimension reduction analysis was performed to identify different neoplastic cell populations. Fifteen neoplastic cell populations were identified which were present in almost all patients (Supplementary Figure 2A).

Identification of intermediate filament expression patterns and grouping of cells

Single cell expression data was scaled (mean/standard deviation) to bring the expression of GFAP, NES, VIM and SYNM within the same range. Hierarchical cluster analysis on the scaled data was performed using gplots version 3.1.3 (hclust function) to group cells based on the expression of *GFAP*, *NES*, *VIM*

and *SYNM*. This resulted in the identification of 10 different clusters of cells with different expression patterns of *GFAP*, *NES*, *VIM* and *SYNM*. Annotation of the clusters was performed by manual exploration of the heatmaps. Clusters were defined as followed; cluster 1 *GFAP/VIM* (n = 1175), cluster 2 *SYNM* (n = 501), cluster 3 *GFAP/NES* (n = 525), cluster 4 *SYNM/VIM* (n = 351), cluster 5 *GFAP* (n = 1305), cluster 6 *VIM* (n = 2619), cluster 7 *NES* (n = 755), cluster 8 *SYNM* (n = 330), cluster 9 *NES/VIM* (n = 1500), cluster 10 negative (n = 2817). Filtering of clusters was performed by removing cells in which < 1 raw RNA count of the gene belonging to the cluster was detected, or > 1 raw count of a gene not belonging to the cluster was detected. Cluster 2 (*SYNM*) contained a group of cells which expressed > 1 raw count of *NES* and *VIM* as well and above average normalized expression levels. Cluster 5 (*GFAP*) contained a group of cells which expressed > 1 raw count of *VIM* and above average normalized expression levels. Therefore, cluster 2 and 5 were separated in two clusters each: *SYNM/VIM* and *SYNM*, *GFAP/VIM* and *GFAP*. The manual filtering and splitting as described above resulted in the 12 cell clusters which were used for further analysis (Supplementary Table 1). Each IF gene significantly marked the cell cluster (Supplementary Table 1). IF gene expression scores were generated by calculating the sum of normalized IF gene expression levels. Cells were defined as having an IF gene signature predicted to result in filament formation in cells ('filaments') when raw counts for *VIM* or *GFAP* were > 1. All other cells (raw counts for *VIM* or *GFAP* < 1) were defined as cells with a signature predicted to result in the expression of soluble IF proteins unable to organize into filaments.

Differential gene expression analysis and gene ontology analysis

Differential gene expression analysis between IF cell clusters was performed using Seurat version 4.1.3 (FindAllMarkers function). Genes were considered significantly lower expressed at $\log_{2}FC < -0.25$ and an adjusted p-value < 0.05, and significantly higher expressed at $\log_{2}FC > 0.25$ and an adjusted p-value < 0.05 (Supplementary Table 2). Gene ontology (GO) analysis was performed to determine overrepresentation of the significantly higher and lower expressed genes in GO clusters biological function using the topGO package (version 2.64.0)⁴⁸. To test for overrepresentation, Fisher statistical test was performed with a weighted algorithm to correct for dependency between parent-child relations between gene ontology clusters. Annotation build of March2023 (org.Hs.eg.db) was used. P-values were adjusted for multiple comparisons using the Bonferonni correction. GO clusters with adjusted p-value < 0.05, min. of 20 significantly overrepresented genes and a fold change of significant/expected genes > 1 were selected as most GO clusters of interest.

Module Score calculations

To compare levels of functional gene expression programs in GBM cells, Seurat v.4.3.0 was used to calculate gene expression Module Scores (AddModuleScore function). The migration gene expression program included all genes significantly different between IF cell groups (Supplementary Table 3) and

present within the GO cluster GO:0030335. The cell periphery marker module score was calculated from the expression of all genes significantly different between IF cell groups (Supplementary Table 2) and upregulated in the peripheral neoplastic cells as determined from analysis of the Darmanis et al., (2017) dataset. Genes were identified as tumor periphery markers at $\log_{2}FC > 0$ and $p_{\text{val_adj}} < 0.05$ (Supplementary Table 4). The invasion score gene expression program was derived from Yu et al., (2020)³⁸.

Module scores for cells with a 'no filaments' and 'filaments' IF gene expression signature were calculated using the largest available integrated GBM single cell RNA sequencing dataset, Glioblastoma Map²³. The Seurat object containing integrated and annotated data was used (<https://zenodo.org/record/6962901#.ZCLLj3ZBxmN>, azimuth_core_GBmap.rds). Cells were grouped as described above into 'no filaments' and 'filaments' cells and module scores were calculated per cell. Statistical analyses between all module scores were performed on patient averages.

Cell culture

U251-MG cells were cultured in growth medium containing Minimum Essential Medium with GlutaMax (Gibco) supplemented with 10% FCS (Eurobio Scientific), 1% penicillin-streptomycin (Gibco) and 1% Non-Essential Amino-Acids (10 mM of each amino acid, Gibco) under 5% CO₂ at 37 °C. All experiments were performed in growth medium unless otherwise specified.

CRISPR/Cas9 gene editing

Guide RNAs (sgRNAs) were designed to target *Vimentin* using the Benchling CRISPR Guide RNA Design Tool. Guide RNAs with high on-/off-target ratios for different exons were chosen. The pSpCas9(BB)-2A-GFP plasmid (PX458, Addgene, Catalog #48138) containing a gRNA scaffold under the U6 promoter and Cas9 and EGFP under the CMV promoter was linearized with BbsI-HF (NEB) and specifically designed annealed oligonucleotides containing the guide sequences (exon 1: 5'-CACCGAACTTCTGCAGCCTTTGGAG -3' and 5'-AAACCTCCAAAGGCTGCAGAAGTTC -3', exon 2: 5'-CACCGGAGGAGATGCTTCAGAGAG -3' and 5'-AAACCTCTCTGAAGCATCTCTCC -3', exon 3: 5'-CACCGAAGATTCCAATTTGCGTTCA -3' and 5'-AAACTGAACGCAAAGTGGAATCTTC -3', exon 4: 5'-CACCGGCAGCCGTGAGGTCAGGCT-3' and 5'-AAACAGCCTGACCTCACGGCTGCC -3') were ligated into the linearized plasmid using T4 Ligase (Thermo Fischer Scientific).

U251 GBM cells were transfected with the sgRNA-containing plasmids by electroporation in Mirus (Lonza) transfection solution with a Nucleofector device (Lonza). Cells were plated in culture dishes and maintained for three days. GFP-positive cells were subsequently collected using fluorescent activated cell sorting (FACS) and subsequently grown till confluency. Vimentin knockdown was determined using western blot analysis. Targeting vimentin exon 2 resulted in a complete loss of

vimentin in all GFP-sorted cells. This pool of vimentin exon 2 Cas9-targeted cells was used for all subsequent analyses.

Lentivirus production

To produce lentiviral particles, 7×10^6 HEK 293T cells were used. 10 μ g 2nd generation packaging plasmid psPAX2, 5 μ g of viral envelope plasmid pMD2.G and 10 μ g of plasmid of interest (pLKO.1-puro, pGK-GFP or pHR-SIN plasmids) were transfected using CaCl_2 in 20 mM HEPES. 48 hours post-transfection, virus was harvested. Viral particles were concentrated using ultracentrifugation (Beckman Coulter, Optima XPN-80) for 1.5 h at 19,000 rpm at 4 °C. Viral particle droplets were added to the medium of targeted cells at a 1 in 5000 dilution.

Lentiviral transduction and generation of stable cell lines

Lentiviral constructs expressing short hairpin RNAs (shRNA) targeting human MMP14 or pLKO.1-puro non-target shRNA (shCTL) were obtained from the Sigma Mission shRNA library. Lentiviral constructs expressing mKate2 (pGK-mKate2) were used. Cells were transduced with lentiviral particles for 24 hours and 48 hours after transduction infected cells were selected. shRNA expressing cells were selected by treatment with 3 μ g/ml puromycin. Fluorescent cells expressing mKate2 were obtained using FACS. Two different shRNA sequences targeting MMP14 were selected from the Sigma Mission library and tested. The sequence inducing the most protein depletion was used for further experiments.

In vivo invasion assay

In vivo analysis of U251 GBM cells invading the zebrafish brain was performed as previously described²⁸. In short, zebrafish larvae of Tg(fli1a:gfp) and Tg(gfap:gfp) line to mark endogenous blood vessels and neural stem cells/astrocytes respectively, were obtained from fertilized zebrafish eggs 3 days prior to xenotransplantation. Larvae were made transparent by preventing melanin pigmentation using N-phenylthiourea (PTU) (0.003% final). Larvae of 3 dpf were mounted in 2.5 mm wide V-shaped agarose trenches and microinjected after 160 mg/L tricaine treatment using a mechanical micromanipulator (CellTram oil vario microinjector, 5176000.025, Eppendorf) with control and IF-depleted U251 cells expressing mKate2. 2.5 % of an 80 % confluent 10 cm Petri dish of U251 cells in 5 μ l PBS was microinjected into the zebrafish Optic Tectum just above the Middle Cerebral Vein at a maximum of 100 μ m from the surface. Successful injection was validated using a fluorescent stereomicroscope after transfer of the larvae to a 24-well plate containing mineral source water with N-Phenylthiourea (PTU, Sigma-Aldrich, P7629-25G) and methylene blue medium. Xenografts containing a single tumor mass formed by 20-50 cells located in the top 200 μ m from the Optic Tectum were selected. After 4 hours of recovery at 32 °C, the larvae were mounted for imaging in a 1% low-melting agarose solution in a 35 mm diameter glass-bottom video-imaging dish. A Nikon Ti2E spinning-disk confocal microscope

equipped with an sCMOS camera (pixel size 6.5 μm , 2048 x 2044 pixels), long working distance 40x water immersion objective and temperature-controlled environment chamber was used to image the tumor cell mass and invaded cells at 4h and 72h post-injection. Z-stacks starting at the most dorsal part of the Optic Tectum and ending below the whole tumor cell mass deeper into the brain were generated. After imaging the larvae were removed from the agarose and transferred to a 24-well plate containing mineral source water with PTU and methylene blue medium and maintained at 32 °C. The Imaris software was used to segment the cells and calculate the 3D area occupied by the tumor cell mass and invaded cells. The invasion index was calculated from the ratio between the 3D area at 72 hours compared to the 3D area at 4 hours.

Hydrogel invasion assays

U251 GBM spheroids were generated by placing dissociated cell suspensions in glioma stem-cell medium containing 50% DMEM:F12 (Gibco) and 50% Neurobasal medium (Gibco) supplemented with B27 (0.5 \times , Invitrogen), human recombinant bFGF and EGF (50 ng/ml each, R&D Systems) and 1 % penicillin-streptomycin in low-adherent T25 culture flasks. These culture conditions allowed for the formation of spheroids. Mixed spheroids were generated from cell suspensions containing both control-mKate2 labelled and ko unlabelled cells, or *vice versa*. After 5 days, spheroids were collected and embedded in Matrigel hydrogels. Spheroids were embedded in 50% or 75% Matrigel at 4 °C. 20 μl drops of Matrigel and cells were placed on glass bottom culture dishes (MatTek) and immediately polymerized at 37 °C for 45 min. Medium, medium supplemented with 10 μM GM6001 in DMSO or medium supplemented with 10 μM DMSO was added to the Matrigel hydrogels before imaging was started. Images were obtained every 10 min for 40 h with an inverted ECLIPSE Ti2 Nikon epifluorescence microscope, equipped with a temperature-controlled environment chamber and x20 NA 0.75 air objective. Images were recorded on a sCMOS PCO edge camera (Photometrics) using the MetaMorph software.

Collagen degradation assay

Spheroids were embedded in 50 μl of 2.0 mg/ml rat tail collagen I (Corning) mixed with 1 \times MEM and Alexa Fluor 647-conjugated type I collagen. The mix was adjusted to pH 7.5 using 0.34 N NaOH and 25 μM HEPES. Collagen was polymerized at 37 °C for 30 min after which medium or medium with 55g/L High molecular weight (MW) Dextran (MW 450000 – 650000, 31392, Sigma) was added. After 16h, samples were fixed in 4% PFA at 37 °C for 30 min and incubated for 2h at 4°C with anti-Collagen I-3/4C antibodies (AdipoGen Life Sciences AG-25T-0116) (cleaved collagen) for 2 h and subsequently counterstained with Cy3 anti-rabbit IgG (Jackson ImmunoResearch, 715-165-151) and DAPI⁴⁹. Images were acquired using a LSM 700 confocal microscope with a plan-Apochromat 40x/1.4 Oil objective.

Collagenolysis was quantified measuring the mean intensity (mean grey value) of Collagen I-3/4C immunostaining in 4.46 μm width linescans drawn around spheroids edges.

Migration in PDMS microchannels

Silicon wafer moulds were specifically designed and fabricated by SU-8 photolithography (Microchem). Polydimethylsiloxane (PDMS) microfluidic devices were generated by mixing the two components of the Clear Silicone Rubber Compound kit (Momentive RTV 615) according to the manufacturer's protocol and addition of the mixture to the moulds. The mixture was degassed using a vacuum chamber and the PDMS was baked at 70°C for 1 h. The PDMS was removed from the moulds, cut to size, and 3 mm diameter holes were generated in the PDMS which served as cell-seeding wells from which the cells could enter the channels. PDMS and a glass FluoroDish (World Precision Instruments FD35-100) were plasma-treated (Harrick Plasma) for 30 s and the PDMS device was placed on the coverslip before incubation at 70°C for 10 min. Channels were plasma treated for 30 s and coated with 25 $\mu\text{g}/\text{mL}$ in PBS fibronectin (Sigma Aldrich F1141-1MG) for 1 h at RT. Excess fibronectin was removed by three PBS washes. Cells labelled for 16 h with SiR-DNA (1:1,000, Tebu-Bio, Spirochrome AG, SC007 SiR-DNA kit) and CellTracker Red CMTPX (1:10,000, Invitrogen C34552) were seeded (10×10^3) in the microwells and allowed to adhere for 2 – 3 h. Medium was added to cover the device and live cell imaging was started after 24 h of cell seeding. Images of living cells were obtained every 10 min for 40 h with a Nikon inverted ECLIPSE Ti2 epifluorescence microscope, equipped with a x20 NA 0.75 air objective and recorded on a sCMOS PCO edge camera (Photometrics) and MetaMorph software.

Microplate rheology

Measurements were performed on cells in glioma stem cell medium (DMEM/F12:Neurobasal supplemented with EGF, FGF, B27 and p/s). The single cell rheology was performed using a set-up described previously⁵⁰. In brief, two glass microplates, a rigid and a flexible one, were used to catch the cell. To avoid cell adhesion, the glass microplates were immersed for 45 min in a solution of pluronic F127 at 2% w/w. Thanks to a computer-controlled piezoelectric stage oscillations in the frequency range of 0.1 Hz to 6.4 Hz were applied to the flexible microplate. The measurement of the deflection of the flexible plate gives the stress $\sigma(t)$ applied to the cell and the resulting strain $\varepsilon(t)$. The dynamic modulus $E(\omega)$ is defined from the ratio $\sigma(t) / \varepsilon(t)$ and can be expressed as $E(\omega) = E'(\omega) + E''(\omega)$, where $E'(\omega)$ and $E''(\omega)$ are the storage and the loss moduli respectively. E' and E'' can be deduced from the amplitude and the phase of the two signals $\sigma(t)$ and $\varepsilon(t)$. The shear modulus is obtained from the formula $G = E / 2(1 + \nu)$ where ν is the Poisson coefficient. Following previous analyses³¹, we took $\nu = 0.3$. To compare the rheological properties of the control cells and the IF depleted cells we used a power law to fit the G' and G'' data over the whole frequency

range ($G'(w) = G_0'w^\alpha$, $G''(w) = G_0''w^\alpha$). The averaged values of G , G' and G'' were calculated at $w = 1 \text{ Hz}$.

Stress relaxation experiment

Measurements were performed on cells in glioma stem cell medium (DMEM/F12:Neurobasal supplemented with EGF, FGF, B27 and p/s). Here, we used the stress relaxation experiment to measure the maximal force necessary to deform the cell from its initial size (10-15 μm) to 3 μm . The cell was initially caught between the two microplates (see section microplate rheology). Then, a constant deformation was applied by displacing the rigid microplate (Figure 5A). To keep a constant cell size (3 μm), the tip of the flexible microplate was maintained at the same position (the position was monitored by an optical sensor) by adjusting the deflection δ of the basis of the flexible plate (due to the computer-controlled piezoelectric holder). The force necessary to deform the cell is proportional to the deflection of the flexible microplate, $F = K\delta$, where K is the stiffness of the flexible microplate. The stress σ is equal to a force divided by an area, $\sigma = F / A$, where A is the contact area of the cell on the microplate.

Microbead rheology with optical tweezers

Microbead rheology with optical tweezers was performed as described previously⁵¹. Briefly, a single fixed optical trap was built by coupling a 1060-1100 nm infrared laser beam (IPG Photonics; 1W laser output power, corresponding to 150 mW on the sample, trap stiffness k_{trap} between 200 and 280 $\text{pN}\cdot\mu\text{m}^{-1}$ calibrated by the Stokes drag force method) to the back port of an inverted Eclipse microscope (Nikon) equipped with a resonant laser confocal A1R scanner (Nikon), a 37°C incubator, and a nanometric piezostage (Mad City Labs). U251 GBM cells were cultured on glass bottom dishes (MatTek) and incubated for 48 hours with fluorescent 2 μm -diameter microspheres in order to obtain typically one to three internalized beads per cell.

Viscoelastic relaxation experiments in the cytoplasm

Viscoelastic step relaxation experiments were performed as described previously^{32,51}. Briefly, a 2 μm -diameter bead was first trapped by the optical tweezers. Following a $X_s = 0.5 \mu\text{m}$ step displacement of the stage, the bead was moved out of the trap center due to the viscoelasticity of its microenvironment. As the optical tweezers acts as a spring on the bead, the bead position $x_b(t)$ relaxes from its maximal position X_b , termed bead step amplitude, toward the center of the optical trap. Relaxation curves $x_b(t)$ during a duration $T = 10 \text{ s}$ are analysed using a phenomenological approach and a viscoelastic standard linear liquid (SLL) model analysis as described previously^{52,53}. The phenomenological approach gives the bead step amplitude X_b and the rigidity index RI defined as $RI = (\int_0^T x_b(t)dt) / (X_s T)$ so that $RI \rightarrow 0$ corresponds to a very soft and deformable cytoplasm while

$RI \rightarrow 1$ corresponds to a very stiff and rigid cytoplasm. The SLL model yields the spring constant K and the viscosity η .

Nucleus indentation experiments

The intracellular microrheology set-up was used to deform nuclei directly *in cellulo* and probe their mechanical properties as described in ³². Briefly, an internalized bead initially in contact with the nucleus (visualized with Hoechst) was trapped in the centre of the optical tweezers. The nucleus was then pushed against the bead by moving the stage at a constant velocity corresponding to a 2.5 μm displacement in 1 min (Supplementary Figure 4A). In a first phase, the trap applied a spring force on the bead, keeping the bead inside the optical trap. As the nucleus moved against the bead, the bead indented the nucleus. The maximal indentation depth was measured by image analysis using ImageJ. When the force applied by the nucleus on the bead became larger than the spring force of the trap, the bead was ejected out of the trap and the nucleus relaxed towards its initial shape (relaxation phase). The time at which ejection occurred (corresponding to the time at the maximum indentation) was measured. The positions of the centre of mass of the bead relative to its initial position $x_b(t)$ and of the centre of mass of the nucleus relative to its initial position $x_n(t)$ were tracked using a home-made Matlab code. The spring constant K_n and viscosity η_n of the nucleus were obtained by fitting

$$x_n(t) - x_b(t) \text{ with a viscoelastic (Kelvin-Voigt) model: } x_n(t) - x_b(t) = \frac{k_{trap}}{k_{trap} + K_n} v_0 \tau \left(\frac{t}{\tau} - \left(1 - e^{-\frac{t}{\tau}} \right) \right)$$

with $\tau = \frac{6\pi R \eta_n}{k_{trap} + K_n}$.

Force transmission to the nucleus

A 2 μm diameter green fluorescent bead located between 0.9 μm and 5 μm from the nucleus labelled with Hoechst was trapped in the fixed optical tweezers. The piezo stage was displaced along the x- or y-direction following a sinusoidal signal of 0.5 μm amplitude and 1 Hz frequency. 512x512 pixels time lapse confocal movies of the bead and nucleus were acquired for 1 min at 7.7 frames per second with the Nikon NIS software in the nd2 format. The 1 Hz oscillatory displacement of the bead in the cytoplasm induced a deformation of the nucleus edge facing the bead at the same frequency, indicating that forces are transmitted to the nucleus through the cytoplasm. The two-channel time lapse movie was then treated using ImageJ and a homemade Matlab code to quantify the displacement of the nucleus edge according to the following protocol. The nd2 movie was converted to 8 bits RGB and the green and blue channels were merged, followed by a 'smooth' filter and a 'enhance contrast' filter. The ImageJ Template Matching (TM) plugin was used to produce a movie in the reference frame of the nucleus (called 'TM movie' in the following). A rectangular region including the nucleus edge opposite the bead was taken as the landmark region of interest in the 'Align slices in stack' macro of

the TM plug in. In the TM movie, a line going through the center of the bead and inside the nucleus was drawn from the bead towards the nucleus in the direction of the oscillations. A kymograph along this line was generated using the Multi Kymograph tool in ImageJ with a line width of 11 pixels. To measure the frequency of oscillations of the bead and of the nucleus edge from the kymograph, two intensity profiles (line width 9 pixels) were plotted: the first along a vertical (time axis) line parallel to the bead edge and the second along a vertical line parallel to the nucleus edge. To measure the amplitude of oscillations of the bead and the nucleus, two supplementary intensity profiles (line width 150 pixels) were drawn in the kymograph to later convert intensity signals into distances: one along a horizontal (distance axis) line from the gap between the bead and the nucleus to the bead and the other along a horizontal line from the gap between the bead and the nucleus to the nucleus edge. The four intensity profiles were then input into a homemade Matlab code which converted the intensity signals into distances and computed the amplitude of the oscillations of the bead and of the nucleus edge at 1Hz using a Fourier transform algorithm. After Fourier transform, the bead signal and, in most cases, the nucleus signal exhibited a peak at 1Hz which was detected by the algorithm. The peak values were termed 'bead amplitude' and 'nucleus deformation' respectively. When no significant peak was detected in the nucleus signal, the value of the Fourier transform at 1Hz was used as the nucleus deformation. The ratio of the nucleus deformation relative to the bead amplitude was used as a proxy for force transmission from the bead to the nucleus.

Micropatterning

Coverslips (19 x 19 mm, 0.13-0.17 mm thickness) were plasma-cleaned for 45 s and incubated with 0.1 mg ml⁻¹ poly-L-lysine/polyethylene glycol (PLL-PEG, Graft Ratio 3.5, PLL MW 20000, PEG MW 2000, JenKem) diluted in 10 mM HEPES, pH 7.4, for 1 h at room temperature. Excess PLL-PEG was allowed to slide down by gravity and coverslips were dried by dipping in H₂O and stored at 4 °C. Micropatterns were printed on PLL-PEG coated coverslips using deep UV and chrome mask containing 1000 μm² crossbow shapes. Patterns were coated with 50 μg/ml fibronectin in fresh NaHCO₃, pH 8.3, for 30 min at room temperature and washed three times in NaHCO₃. 40 x 10³ cells were immediately plated on coated crossbow-shaped micropatterns and allowed to adhere for 16 h before fixation.

Real-time 3D nuclear deformation analysis

GBM spheroids were embedded in 75% Matrigel and 20 μl hydrogel drops were placed on glass-bottom dishes. Hydrogels were polymerized at 37 °C for 45 min. Spheroids were labelled with SiR-DNA (1:1,000, Tebu-Bio, Spirochrome AG, SC007 SiR-DNA kit) and CellTracker Red CMTPX (1:10,000, Invitrogen C34552) in medium for 16 h. Live imaging was started at 24 h after cell embedding in hydrogel. Labelled cells were imaged for 5 min with a Nikon Ti2E spinning-disk confocal microscope

equipped with an sCMOS camera (pixel size 6.5 μm , 2048 x 2044 pixels), long working distance x40 water immersion objective, and temperature-controlled environment. Images were taken at a 1 μm z-resolution and maximum speed. Images were analyzed to deduce nuclear deformation measurements according to a new analysis method developed to obtain deformation from the optical flow of fluorescent molecules⁵⁴. In short, the nuclei of migrating cells are first tracked and segmented with a combination of hierarchical K-means clustering (for initialization) and Active Contours. The movement within each nucleus is then extracted at the “pixel” level with a technique called optical flow, resulting in a vector field of displacements per time frame. However, so-called “rigid” displacements such as translations and rotations do not induce nuclear strain nor deformation. To instead assess the part of the displacements involving deformation, we compute the second order strain tensor from the relative motion of neighboring pixels. The tensor is computed by taking the symmetric part of the spatial derivatives of the displacement. In this way, it reflects whether the different parts of the nucleus move closer together or farther apart at a local level, thereby reflecting compression and extension.

While expressive, the result is a high-dimensional tensor at each point in the nucleus and at each time frame. To derive a single measure of deformation for comparison between populations, we first derive a single value per point by computing the Frobenius norm of the tensor, which weights shear and hydrostatic movements equally. The global deformation measure of each nucleus is then derived by computing the mean value of this local deformation through space and time. The precise mathematical formulation of this approach can be found in the Supplementary Methods.

Preparation of fibronectin coated polyacrylamide hydrogels of different rigidities

The polyacrylamide hydrogels were prepared as described previously described⁵⁵. In short, after plasma-cleaning of coverslips, silanization using 1% (v/v) 3-(trimethoxysilyl)propyl methacrylate and 1% (v/v) acetic acid in ethanol, coverslips were washed twice in ethanol and dried. Solutions with different proportions of acrylamide and bisacrylamide^{56–58} were used to generate substrates of different rigidities in 4-(2-hydroxyethyl)-1-piperazineethanesulfonic acid (HEPES) buffer. After addition of 2.5 μl 10% ammonium persulfate (APS) and 0.25 μl tetramethylethylenediamine (TEMED) 50 μl solutions were allowed to polymerize in between a 20 x 20 (bottom) and 18 x 18 (top) coverslip for 1 hour at room temperature. The top glass was removed after addition of HEPES and the polymerized gel was activated with ultraviolet light for 5 min using Sulpho-SANPAH. Gels were washed twice in HEPES and coated with 50 $\mu\text{g}/\text{ml}$ fibronectin for 1 hour at 37 $^{\circ}\text{C}$. Excess fibronectin was removed by washing once in PBS and 40 x 10³ cells were plated on the coated hydrogels.

Immunostaining

Cells were fixed in 4% paraformaldehyde (PFA) or 2% PFA for MMP14 immunostainings. A fixation time of 15 min at room temperature was used for cells on 2D coverslips. Cells in 3D Matrigel and PDMS microchannels were fixed for 30 min at room temperature. Cells were permeabilized for 5 min with 0.1 % Triton X-100 (except for MMP14 immunostainings) and blocked for 1 h with 5% bovine serum albumin (BSA) in PBS. Primary antibody incubation was performed in 3% BSA in PBS for 1 h at room temperature (coverslips) or for 16 h at 4 °C (gels on coverslips, PDMS microchannels). Secondary antibody incubation was performed in 3% BSA in PBS for 1 h at room temperature together with labelling of the nuclei with Hoechst 33342 (1:10,000 of 10 mg/mL stock solution, Thermo Scientific Pierce) and the actin cytoskeleton with Alexa 647 phalloidin (1:2000, lot GR3256003-6, Abcam). Coverslips, gels on coverslips, and PDMS channels were mounted in Prolong Diamond (Invitrogen, P36961).

Primary antibodies used were anti-GFAP (1:500, Z0334, rabbit polyclonal, Dako), anti-Nestin (1:1,000, MAB1259, mouse monoclonal, R&D Systems), anti-Vimentin (1:500, sc-6260, mouse monoclonal Santa Cruz Biotechnology), anti-Synemin (1:1,000, sc-374484, mouse monoclonal, Santa Cruz Biotechnology), anti-YAP (1:1,000, sc-101199, mouse monoclonal, Santa Cruz Biotechnology), anti-MMP14 (1:500, ab51074, rabbit monoclonal, Abcam), anti-Collagen I-3/4C (cleaved collagen) (AdipoGen Life Sciences AG-25T-0116). Secondary antibodies used were Alexa Fluor 488 donkey anti-mouse (715-545-151, Jackson ImmunoResearch), rhodamine (TRITC) donkey anti-mouse (715-295-150, Jackson ImmunoResearch), Alexa Fluor 488 donkey anti-rabbit (711-545-152, Jackson ImmunoResearch), rhodamine (TRITC) donkey anti-rabbit (711-025-152, Jackson ImmunoResearch). Images were acquired with a Leica DM6B epifluorescent microscope equipped with a x40 1.25 NA and x63 1.4 NA oil objective and recorded on a CCD Leica DFC3000G camera with Leica Application Suite X Software, a Nikon Ti2E spinning-disk confocal microscope or Leica SP8 confocal microscope.

Western blot

Cell lysates were obtained with NuPage LDS sample buffer (Invitrogen) supplemented with 50 mM dithiothreitol and protease inhibitor (cOmplete cocktail, Roche 11 873 588 001). Samples were boiled for 5 min at 95 °C before loading on polyacrylamide gels (4-12% Bis-Tris Gel, Invitrogen). Proteins were separated by gel electrophoreses at 120 V and transferred at 100 V for 1 h on nitrocellulose or PVDF membranes. Membranes were blocked with Tris-buffered saline, 0.1% Tween 20 detergent (TBST) and 5% milk and incubated for 1 h at RT with primary antibody and 1 h at RT or 16 h at 4 °C with horseradish peroxidase (HRP)-conjugated secondary antibody in 5% milk in TBST. Protein bands were revealed with

ECL chemoluminescent substrate (Biorad) and signals were recorded using a ChemiDoc MP Imaging System (Biorad).

The primary antibodies used were anti-GFAP (1:2,000, Z0334, rabbit polyclonal, Dako), anti-Nestin (1:1,000, MAB1259, mouse monoclonal, R&D Systems), anti-Vimentin (1:2,000, sc-6260, mouse monoclonal Santa Cruz Biotechnology), anti-Synemin (1:1,000, sc-374484, mouse monoclonal, Santa Cruz Biotechnology), anti-GAPDH (1:10,000, MAB374, mouse monoclonal, EMD Millipore), anti-MMP14 (1:1,000, ab51074, rabbit monoclonal, Abcam). Secondary antibodies used were HRP donkey anti-mouse and goat anti-rabbit (both 1:10,000, Jackson ImmunoResearch).

Western blot signals were quantified using ImageJ. Equal areas were defined for each lane and mean intensities of protein bands were measured. All signals were normalized by their loading control GAPDH signal.

RNA isolation, cDNA generation and quantitative real-time qPCR

RNA was extracted using standard TRIzol (Thermo Fisher Scientific) chloroform extraction methods. RNA concentration and purity were measured using a spectrophotometer (NanoDrop). 500 ng of RNA was used to prepare cDNA using QuantiTect Reverse Transcription Kit (Qiagen) according to the manufacturer's protocol. The generated cDNA was used for real-time quantitative PCR (Applied Biosystems™ StepOne™ Real-Time PCR System) using SYBR Green Master mix (Applied Biosystems™) using the primers for *GFAP* (forward: 5'- GACCTGGCCACTGTGAGG -3', reverse: 5'- GGCTTCATCTGCTTCCTGTC -3'), *VIM* (forward: 5'- CGTACGTCAGCAATATGAAAGTGTG -3', reverse: 5'- TCAGAGAGGTCAGCAAACCTGGA -3'), *SYNM* (forward: 5'- GAGGAGTACGGGATACAGGCC -3', reverse: 5'- GAGGTCCTGATAGTCCCGCA -3'), *NES* (forward: 5'- GATCTAAACAGGAAGGAAATCCAGG -3', reverse: 5'- TCTAGTGCTCATGGCTCTGGTTTT -3'), *GAPDH* (forward: 5'- TGCACCACCAACTGCTTAGC -3', reverse: 5'- GGCATGGACTGTGGTCATGA -3'), *Alu* (forward: 5'- CAACATAGTGAAACCCCGTCTCT -3', reverse: 5'- GCCTCAGCCTCCCGAGTAG -3'), *MMP14* (primer pair 1: forward: 5'- CGGAGAATTTTGTGCTGCCC -3', reverse: 5'- AACCTGACTCACCCCATATA -3' and primer pair 2: forward: 5'- GGAGAATTTTGTGCTGCCCCG -3', reverse: 5'- GAACCCTGACTCACCCCATATA -3').

A threshold was set on the amplification curves for each individual primer and resulting Ct values were transformed (2^{-Ct}) and normalized to the mean value of the transformed Ct values of the reference genes GAPDH and Alu element Jurke (Alu-J).

Image analysis

Nuclear translocation of YAP

The YAP nuclear/cytoplasmic ratio was determined using Image J. After subtraction of background fluorescence, the nucleus and cytoplasm were outlined manually and the mean grey value of the nucleus and cytoplasm was measured. The ratio was calculated as followed:

$$YAP \text{ nuclear / cytoplasmic ratio} = \frac{\text{Mean grey value YAP in the nucleus}}{\text{Mean grey value YAP in the cytoplasm}}$$

In vivo invasion index

The *in vivo* invasion index was calculated from the 3D area occupied by the tumor cell mass and invaded cells at 4h and 72 hours after injection.

$$Invasion \text{ index} = \frac{3D \text{ area at 72 hours}}{3D \text{ area at 4 hours}}$$

Invasion in vitro

Cell invasion analysis into Matrigel was performed by manual measurements of the length (R) of the 15 longest distances from the invaded spheroid core at 40 hours of invasion and the sphere radius at the start of invasion (Supplementary Figure 3D). The radial invasion index (RII) was calculated as followed:

$$RII = \frac{\text{Mean}(R1, R2, \dots, Rn)}{R_0}$$

Detailed analysis of cell invasion analysis into Matrigel was performed by manual tracking of 'invading' cells defined as cells which have lost their lateral cell-cell contacts and have invaded out of the spheroid. The number of invading cells was normalized by the sphere diameter at the start of invasion:

$$Invading \text{ cells } (\mu\text{m}^{-1}) = \frac{\# \text{ invading cells}}{\text{spheroid diameter at the start of invasion } (\mu\text{m})}$$

Leader cells were defined as the first cells leaving the spheroid core and follower cells as the cells leaving the spheroid core behind one or more cells.

$$Leader \text{ cells } (\mu\text{m}^{-1}) = \frac{\# \text{ invading leader cells}}{\text{spheroid diameter at the start of invasion } (\mu\text{m})}$$

$$Follower \text{ cells } (\mu\text{m}^{-1}) = \frac{\# \text{ invading follower cells}}{\text{spheroid diameter at the start of invasion } (\mu\text{m})}$$

In spheroids containing mCherry labelled and unlabelled cells, the number of labelled and unlabelled invaded cells were quantified separately.

Migration in microfluidic devices

Migration speed and transit time through constrictions were based on SiR-DNA signals. An image was taken every 10 minutes.

To obtain the migration speed in microchannels, the nuclei of cells were manually tracked. The mean velocity was calculated according to the following equation for a given (x, y) coordinate of the nucleus:

$$Mean \text{ velocity} = \frac{\text{sum of cell velocities}}{\text{number of time points acquired}}$$

The transit time of the nucleus was calculated as the difference between the exit timepoint and the entry timepoint. Blocked cells were defined as cells for which the transit time was more than 1000 min.

Graphs and statistics

Matlab or Rstudio was used to create all graphs. Rstudio was used to perform statistical analyses. Based on the results of a Levene's test for equality of variances and a Shapiro-Wilk test for normal distribution of the data a parametric or non-parametric statistical test was performed after outliers were removed ($< Q1 - 1.5 \times IQR$ and $> Q3 + 1.5 \times IQR$). Tests used in each figure are indicated in the corresponding figure legend.

Data availability

All the raw data generated during this study are available from the corresponding author on reasonable request.

The single cell RNA sequencing data from Yuan et al., 2018 and Darmanis et al., 2017 are available in the Gene Expression Omnibus under the accession GSE103224 (Yuan et al., 2018) and GSE84465 (Darmanis et al., 2017). The Ruiz-Moreno et al., 2022 integrated single cell RNA sequencing data set (glioblastoma map) is available at <https://zenodo.org/record/6962901#.ZCLLj3ZBxmN>.

References

1. Drumm, M. R. *et al.* Extensive brainstem infiltration, not mass effect, is a common feature of end-stage cerebral glioblastomas. *Neuro Oncol* **22**, 470–479 (2020).
2. Patel, A. P. *et al.* Single-cell RNA-seq highlights intratumoral heterogeneity in primary glioblastoma. *Science* **344**, 1396–1401 (2014).
3. Comba, A. *et al.* Spatiotemporal analysis of glioma heterogeneity reveals COL1A1 as an actionable target to disrupt tumor progression. *Nat Commun* **13**, 3606 (2022).
4. Alibert, C., Goud, B. & Manneville, J.-B. Are cancer cells really softer than normal cells? *Biol Cell* **109**, 167–189 (2017).
5. Pogoda, K. *et al.* Compression stiffening of brain and its effect on mechanosensing by glioma cells. *New J Phys* **16**, 075002 (2014).
6. Pogoda, K. *et al.* Soft Substrates Containing Hyaluronan Mimic the Effects of Increased Stiffness on Morphology, Motility, and Proliferation of Glioma Cells. *Biomacromolecules* **18**, 3040–3051 (2017).
7. Grundy, T. J. *et al.* Differential response of patient-derived primary glioblastoma cells to environmental stiffness. *Sci Rep* **6**, 23353 (2016).

8. Isomursu, A. *et al.* Directed cell migration towards softer environments. *Nat Mater* **21**, 1081–1090 (2022).
9. Miroshnikova, Y. A. *et al.* Tissue mechanics promote IDH1-dependent HIF1 α –tenascin C feedback to regulate glioblastoma aggression. *Nature Cell Biology* **18**, 1336–1345 (2016).
10. Dutour-Provenzano, G. & Etienne-Manneville, S. Intermediate filaments. *Curr Biol* **31**, R522–R529 (2021).
11. Leduc, C. & Etienne-Manneville, S. Intermediate filaments in cell migration and invasion: the unusual suspects. *Current Opinion in Cell Biology* **32**, 102–112 (2015).
12. Mendez, M. G., Kojima, S. I. & Goldman, R. D. Vimentin induces changes in cell shape, motility, and adhesion during the epithelial to mesenchymal transition. *The FASEB Journal* **24**, 1838–1851 (2010).
13. Sivagurunathan, S. *et al.* Expression of vimentin alters cell mechanics, cell-cell adhesion, and gene expression profiles suggesting the induction of a hybrid EMT in human mammary epithelial cells. *Front Cell Dev Biol* **10**, 929495 (2022).
14. Uceda-Castro, R. *et al.* GFAP splice variants fine-tune glioma cell invasion and tumour dynamics by modulating migration persistence. *Sci Rep* **12**, 424 (2022).
15. van Bodegraven, E. J. *et al.* GFAP alternative splicing regulates glioma cell-ECM interaction in a DUSP4-dependent manner. *FASEB J.* **33**, 12941–12959 (2019).
16. De Pascalis, C. *et al.* Intermediate filaments control collective migration by restricting traction forces and sustaining cell-cell contacts. *J. Cell Biol.* (2018) doi:10.1083/jcb.201801162.
17. van Bodegraven, E. J. & Etienne-Manneville, S. Intermediate filaments against actomyosin: the david and goliath of cell migration. *Current Opinion in Cell Biology* **66**, 79–88 (2020).
18. van Bodegraven, E. J. & Etienne-Manneville, S. Intermediate Filaments from Tissue Integrity to Single Molecule Mechanics. *Cells* **10**, 1905 (2021).
19. Qin, Z., Buehler, M. J. & Kreplak, L. A multi-scale approach to understand the mechanobiology of intermediate filaments. *Journal of Biomechanics* **43**, 15–22 (2010).

20. Guo, M. *et al.* The Role of Vimentin Intermediate Filaments in Cortical and Cytoplasmic Mechanics. *Biophysical Journal* **105**, 1562–1568 (2013).
21. Pogoda, K. *et al.* Unique Role of Vimentin Networks in Compression Stiffening of Cells and Protection of Nuclei from Compressive Stress. *Nano Lett.* **22**, 4725–4732 (2022).
22. Louis, D. N. *et al.* The 2021 WHO Classification of Tumors of the Central Nervous System: a summary. *Neuro Oncol* **23**, 1231–1251 (2021).
23. Ruiz-Moreno, C. *et al.* Harmonized single-cell landscape, intercellular crosstalk and tumor architecture of glioblastoma. <http://biorxiv.org/lookup/doi/10.1101/2022.08.27.505439> (2022) doi:10.1101/2022.08.27.505439.
24. Steinert, P. M. *et al.* A high molecular weight intermediate filament-associated protein in BHK-21 cells is nestin, a type VI intermediate filament protein. Limited co-assembly in vitro to form heteropolymers with type III vimentin and type IV alpha-internexin. *J. Biol. Chem.* **274**, 9881–9890 (1999).
25. Jing, R. *et al.* Synemin is expressed in reactive astrocytes in neurotrauma and interacts differentially with vimentin and GFAP intermediate filament networks. *Journal of Cell Science* **120**, 1267–1277 (2007).
26. Darmanis, S. *et al.* Single-Cell RNA-Seq Analysis of Infiltrating Neoplastic Cells at the Migrating Front of Human Glioblastoma. *Cell Rep* **21**, 1399–1410 (2017).
27. Yu, K. *et al.* Surveying brain tumor heterogeneity by single-cell RNA-sequencing of multi-sector biopsies. *National Science Review* **7**, 1306–1318 (2020).
28. Peglion, F., Coumailleau, F. & Etienne-Manneville, S. Live Imaging of Microtubule Dynamics in Glioblastoma Cells Invading the Zebrafish Brain. *J Vis Exp* (2022) doi:10.3791/64093.
29. Vilchez Mercedes, S. A. *et al.* Decoding leader cells in collective cancer invasion. *Nat Rev Cancer* **21**, 592–604 (2021).
30. Bufi, N., Durand-Smet, P. & Asnacios, A. Single-cell mechanics: The parallel plates technique. in *Methods in Cell Biology* vol. 125 187–209 (Elsevier, 2015).

31. Wu, P.-H. *et al.* A comparison of methods to assess cell mechanical properties. *Nat Methods* **15**, 491–498 (2018).
32. Alibert, C. *et al.* Multiscale rheology of glioma cells. *Biomaterials* **275**, 120903 (2021).
33. Hu, J. *et al.* High stretchability, strength, and toughness of living cells enabled by hyperelastic vimentin intermediate filaments. *Proc Natl Acad Sci USA* **116**, 17175–17180 (2019).
34. Patteson, A. E. *et al.* Vimentin protects cells against nuclear rupture and DNA damage during migration. *The Journal of Cell Biology* **218**, 4079–4092 (2019).
35. Elosegui-Artola, A. *et al.* Force Triggers YAP Nuclear Entry by Regulating Transport across Nuclear Pores. *Cell* **171**, 1397-1410.e14 (2017).
36. Dupont, S. & Wickström, S. A. Mechanical regulation of chromatin and transcription. *Nat Rev Genet* **23**, 624–643 (2022).
37. Dolega, M. *et al.* Mechanical behavior of multi-cellular spheroids under osmotic compression. *Journal of the Mechanics and Physics of Solids* **147**, 104205 (2021).
38. Venkataramani, V. *et al.* Glioblastoma hijacks neuronal mechanisms for brain invasion. *Cell* **185**, 2899-2917.e31 (2022).
39. Gritsenko, P. G. *et al.* p120-catenin-dependent collective brain infiltration by glioma cell networks. *Nat Cell Biol* **22**, 97–107 (2020).
40. Bouchet, B. P. & Akhmanova, A. Microtubules in 3D cell motility. *J Cell Sci* **130**, 39–50 (2017).
41. Zaman, M. H. *et al.* Migration of tumor cells in 3D matrices is governed by matrix stiffness along with cell-matrix adhesion and proteolysis. *Proc. Natl. Acad. Sci. U.S.A.* **103**, 10889–10894 (2006).
42. Etienne-Manneville, S. Cytoplasmic Intermediate Filaments in Cell Biology. *Annu. Rev. Cell Dev. Biol.* **34**, 1–28 (2018).
43. Hsia, C.-R. *et al.* Confined migration induces heterochromatin formation and alters chromatin accessibility. *iScience* **25**, 104978 (2022).
44. Mohammadi, H. & Sahai, E. Mechanisms and impact of altered tumour mechanics. *Nat Cell Biol* **20**, 766–774 (2018).

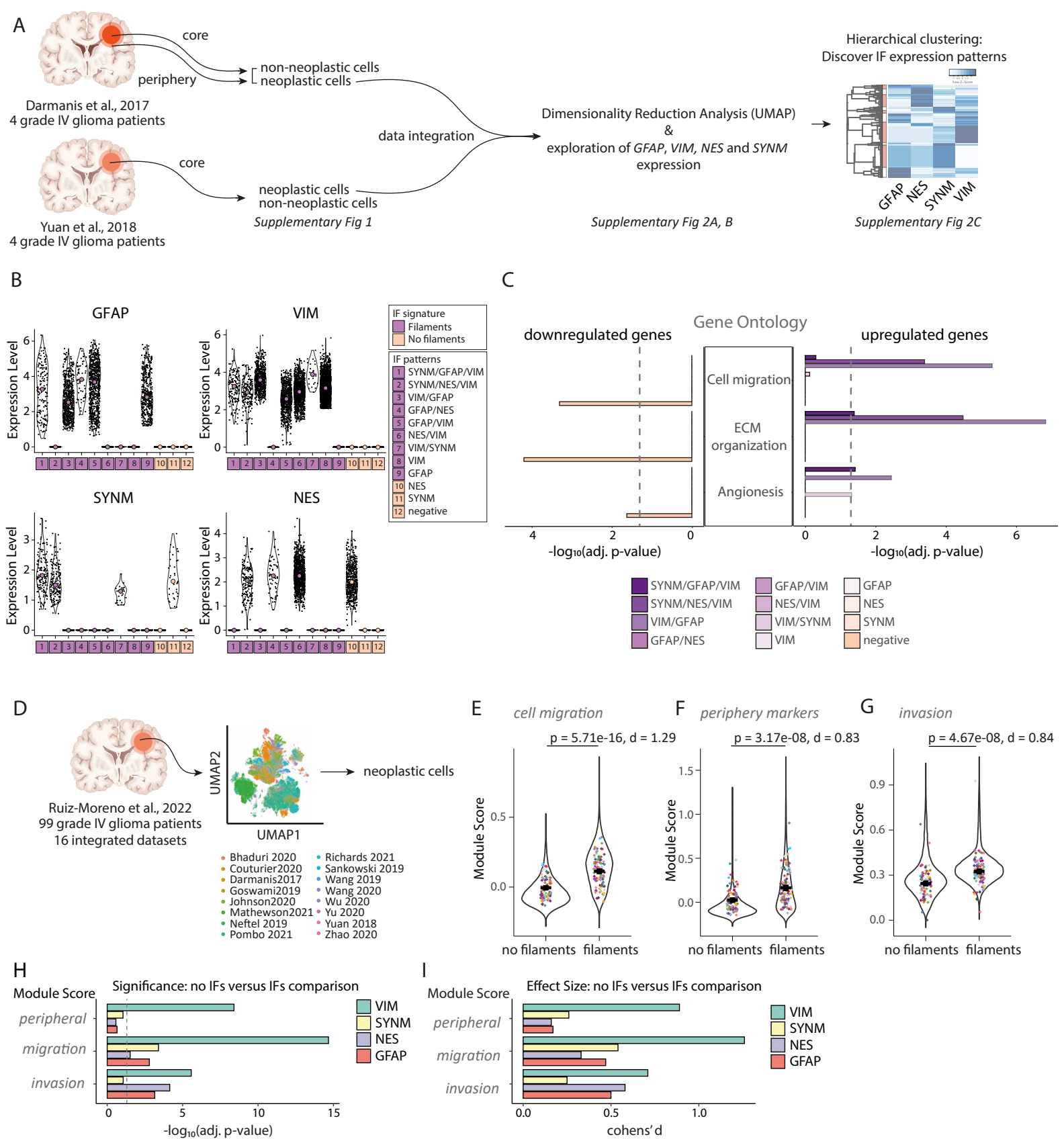
45. Andreu, I. *et al.* Mechanical force application to the nucleus regulates nucleocytoplasmic transport. *Nat Cell Biol* **24**, 896–905 (2022).
46. Moeton, M. *et al.* GFAP isoforms control intermediate filament network dynamics, cell morphology, and focal adhesions. *Cellular and Molecular Life Sciences* **73**, 4101–4120 (2016).
47. Yuan, J. *et al.* Single-cell transcriptome analysis of lineage diversity in high-grade glioma. *Genome Medicine* **10**, (2018).
48. The Gene Ontology Consortium. Gene Ontology Consortium: going forward. *Nucleic Acids Research* **43**, D1049–D1056 (2015).
49. Infante, E. *et al.* LINC complex-Lis1 interplay controls MT1-MMP matrix digest-on-demand response for confined tumor cell migration. *Nat Commun* **9**, 2443 (2018).
50. Desprat, N., Guirouy, A. & Asnacios, A. Microplates-based rheometer for a single living cell. *Review of Scientific Instruments* **77**, 055111 (2006).
51. Guet, D. *et al.* Mechanical role of actin dynamics in the rheology of the Golgi complex and in Golgi-associated trafficking events. *Current Biology* **24**, 1700–1711 (2014).
52. Mandal, K., Asnacios, A., Goud, B. & Manneville, J.-B. Mapping intracellular mechanics on micropatterned substrates. *Proc. Natl. Acad. Sci. U.S.A.* **113**, E7159–E7168 (2016).
53. Mandal, K. *et al.* Role of a Kinesin Motor in Cancer Cell Mechanics. *Nano Lett.* **19**, 7691–7702 (2019).
54. Kesenci, Y. *et al.* PDE-Constrained Optimization for Nuclear Mechanics. in *2022 IEEE International Conference on Image Processing (ICIP)* 2192–2195 (IEEE, 2022).
doi:10.1109/ICIP46576.2022.9897967.
55. Seetharaman, S. *et al.* Microtubules tune mechanosensitive cell responses. *Nat. Mater.* **21**, 366–377 (2022).
56. Trepát, X. *et al.* Physical forces during collective cell migration. *Nature Phys* **5**, 426–430 (2009).
57. Serra-Picamal, X., Conte, V., Sunyer, R., Muñoz, J. J. & Trepát, X. Mapping forces and kinematics during collective cell migration. *Methods Cell Biol.* **125**, 309–330 (2015).

58. Tambe, D. T. *et al.* Collective cell guidance by cooperative intercellular forces. *Nat Mater* **10**, 469–475 (2011).
59. Boquet-Pujadas, A., Olivo-Marin, J.-C. & Guillén, N. Bioimage Analysis and Cell Motility. *Patterns* **2**, 100170 (2021).
60. Dufour, A., Thibeaux, R., Labruyere, E., Guillen, N. & Olivo-Marin, J.-C. 3-D Active Meshes: Fast Discrete Deformable Models for Cell Tracking in 3-D Time-Lapse Microscopy. *IEEE Trans. on Image Process.* **20**, 1925–1937 (2011).
61. Sun, D., Roth, S. & Black, M. J. Secrets of optical flow estimation and their principles. in *2010 IEEE Computer Society Conference on Computer Vision and Pattern Recognition* 2432–2439 (IEEE, 2010). doi:10.1109/CVPR.2010.5539939.

Figure legends

Figure 1 - IF expression in glioblastoma patient samples correlates with a migratory and invasive gene expression signature

A Schematic of the analysis pipeline of Yuan et al., 2018 and Darmanis et al., 2017 datasets to investigate the expression patterns of *VIM*, *NES*, *GFAP* and *SYNM* in neoplastic glioblastoma cells. **B** Violin plots of normalized expression of *VIM*, *NES*, *GFAP* and *SYNM* in the IF expression pattern-groups. Groups are ordered from high (left), to low (right) total IF expression level. Purple groups represent cells with an IF gene expression signature predicted to generate filaments (“filaments”). Light pink groups represent cells with a signature predicted to result in soluble protein expression or no expression of IF proteins (“no filaments”). **C** Significantly overrepresented gene ontology (GO) clusters by downregulated (left) or upregulated (right) genes in one of the 12 IF clusters. Only GO clusters significantly overrepresented (adjusted p-value < 0.05, dotted grey line) in three or more IF cell clusters are shown. **D** Schematic of the analysis of the Glioblastoma Map generated by Ruiz-Moreno et al., 2022 in which 16 datasets single cell RNA sequencing datasets of grade IV glioma (glioblastoma) patient samples were integrated. Cells annotated as neoplastic cells were used for the downstream analysis. **E-G** Violin plots of module scores for significantly different migration-related genes (GO:0030335, Supplementary Table 3) (E), tumour periphery markers (Darmanis et al., 2017; Supplementary Table 4) (F) and invasion markers (Yu et al., 2022) (G) in cells with a ‘no filaments’ or ‘filaments’ IF signature. Coloured diamonds represent the average expression per patient (see Supplementary Figure 2J for patient legend). Two-sided *t*-tests were realised on patient averages ($N = 99$) and the Cohen’s *d* effect size coefficient is given. Error bars represent SEM. **H, I** Results of two-sided *t*-tests on patient averages for *VIM*, *SYNM*, *NES* and *GFAP* negative compared to positive cells on module scores for migration-related genes, tumour periphery markers and invasion markers of E-G.

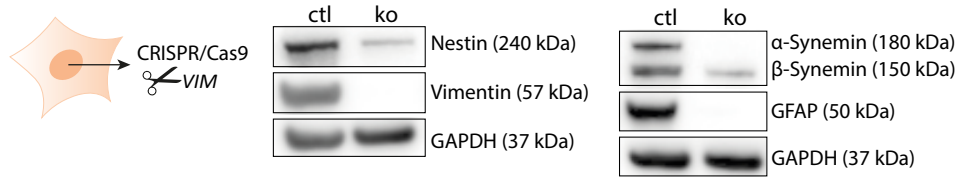


van Bodegraven et al.
Figure 1

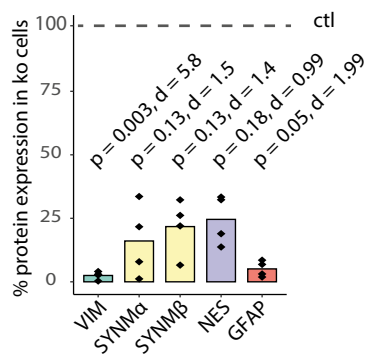
Figure 2 – IF depletion decreases invasion in the *in vivo* zebrafish brain and *in vitro*

A Western blots showing VIM, GFAP, NES, α -SYNM and β -SYNM protein levels in control and genetically modified U251 glioblastoma cells with CRISPR/Cas9 targeting the vimentin gene (ko). **B** Graph showing the percentage of each IF protein expression (normalized to GAPDH) in IF-depleted cells compared to control U251 cells. Coloured bars represent the average and black diamonds individual data points. P-values are the result of a two-sided paired *t*-test on the normalized protein expression values ($N = 4$) and Cohen's *d* effect size coefficient is given. **C** Immunofluorescence images of U251 control (ctl) and IF knockout (ko) cells stained for vimentin (yellow) and labelled with phalloidin (grey) and Hoechst (blue). *Scale bar = 10 μ m*. **D** Immunofluorescence images of U251 control (ctl) and IF-depleted (ko) cells stained for GFAP (red), nestin (green) and labelled with Hoechst (blue). *Scale bar = 10 μ m*. **E** Schematic of glioblastoma invasion assay in the *in vivo* zebrafish brain. **F** Maximum intensity projection of a spinning disk confocal z-stack of an invading trail of mKate2-labelled U251 control cells (in red) into the zebrafish brain with fluorescently labelled neural progenitor cells (in grey). *Scale bar = 20 μ m*. **G** Overview of zebrafish brains injected with fluorescently labelled U251 control or IF-depleted cells in the optic tectum at 4 and 72 hours after injection. Segmented U251 glioma cells are shown in red and zebrafish neural progenitor cells in grey. *Scale bar = 50 μ m*. **H** Graph showing the invasion index of control (ctl) and IF-depleted (ko) cells index 72 hours after injection. An invasion index of > 1 indicates invasion. Circles and squares show individual zebrafish larvae and different tones of colours correspond with zebrafish larvae batches ($N = 9, 8$ fish; two-tailed unpaired *t*-test). **I** Phase-contrast images of ctl and ko GBM spheroids embedded in 75% Matrigel at the start ($t = 0$ h) and after 24 ($t = 24$ h), and 40 hours ($t = 40$ h) of invasion. **J** Graph showing the number of invading cells after 40 hours of invasion in 75% Matrigel normalized by the radius of the sphere at the start of invasion. Grey dots represent individual spheroids ($n = 29, 30$ spheroids). Pink (control spheroids) and blue (IF-depleted spheroids) shapes indicate the averages of biological replicates ($N = 3$, two-tailed unpaired *t*-test). **K** Graph showing the number of cells which have invaded into 75% Matrigel as leader or follower cells at 40 hours of invasion normalized by the radius of the sphere at the start of invasion. Grey dots represent individual spheroids ($n = 29, 30$ spheroids). Pink (control spheroids) and blue (IF-depleted spheroids) shapes represent averages of biological replicates ($N = 3$, two-tailed unpaired *t*-tests). **L** Phase-contrast and fluorescent images of spheroids containing control (ctl) and IF-depleted (ko) cells at the start ($t = 0$ h) and after 40 hours of invasion ($t = 40$ h) in 75% Matrigel. Ctl (top) or ko (bottom) cells were labelled with cytoplasmic mKate2. *Red asterisk = ctl leader cells. Blue asterisk = ko leader cell. Scale bar = 200 μ m*. **M** Quantification of the percentage of control (ctl) and IF-depleted (ko) leader or follower cells invading from mixed spheres (1:1) at 40 hours of invasion. White/pink dots represent the percentage of control cells from individual spheroids ($n = 58$ spheroids). P-values are the result of a two-tailed unpaired *t*-test on the averages of biological replicates ($N = 3$). **N** Quantification of the number of invading IF-depleted leader or follower cells after 40 hours of invasion normalized by the radius of the sphere in the absence (-) or presence (+) of control cells. Grey dots represent individual spheroids ($n = 30, 58$ (leaders), $n = 29, 58$ (followers)). Blue (IF-depleted spheroids without ctl) and grey (IF-depleted spheroids with ctl) shapes represent averages of biological replicates ($N = 3$, two-tailed unpaired *t*-tests). P values along with Cohen's *d* effect size coefficients are indicated. Error bars represent SEM.

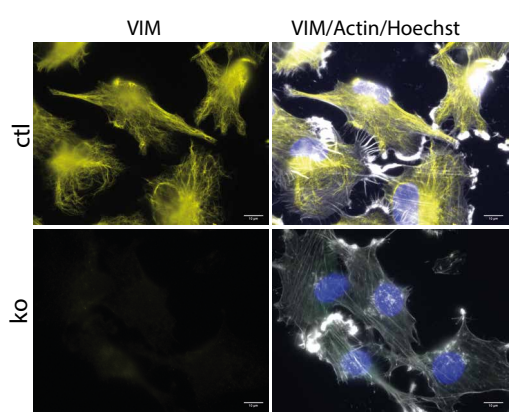
A



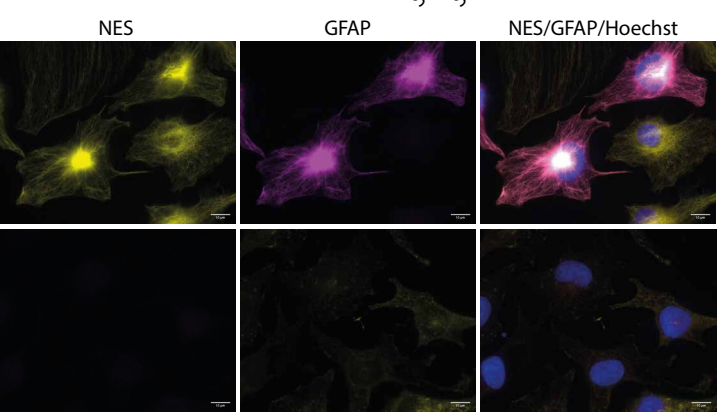
B



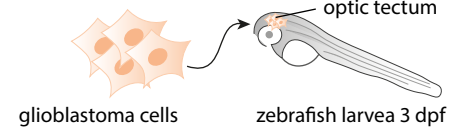
C



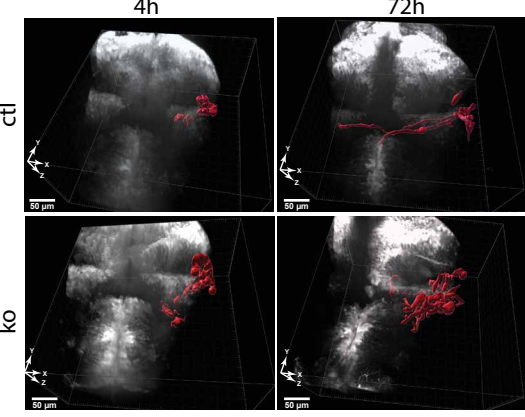
D



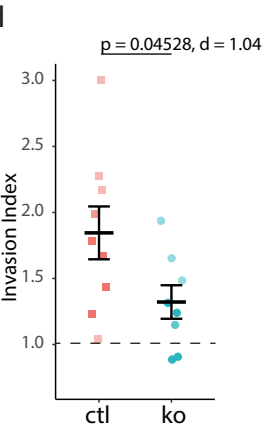
E



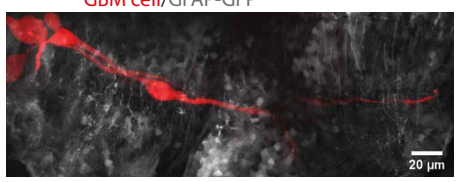
G



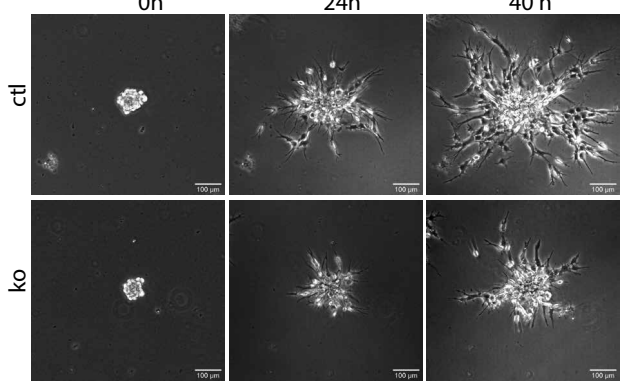
H



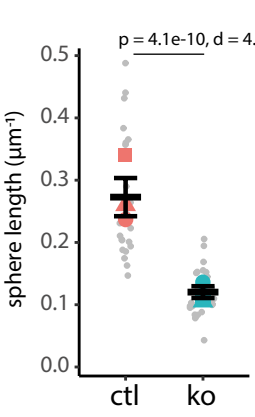
F



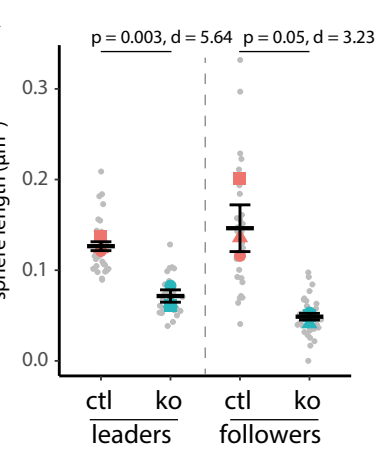
I



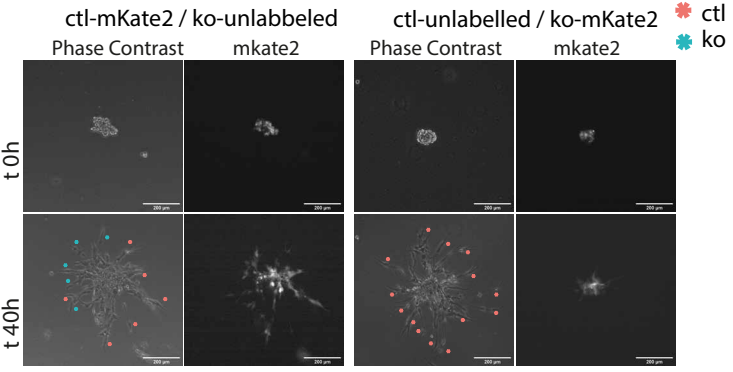
J



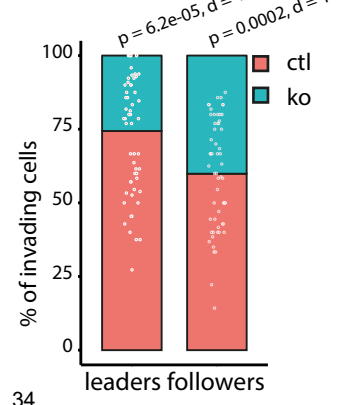
K



L



M



N

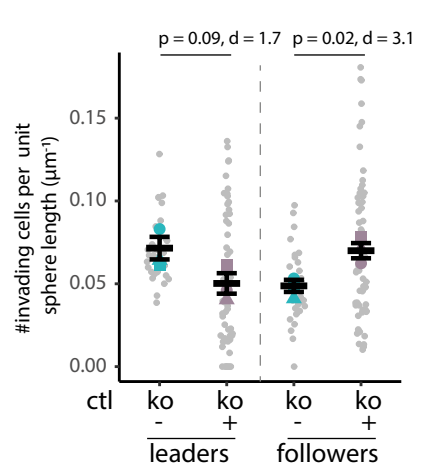
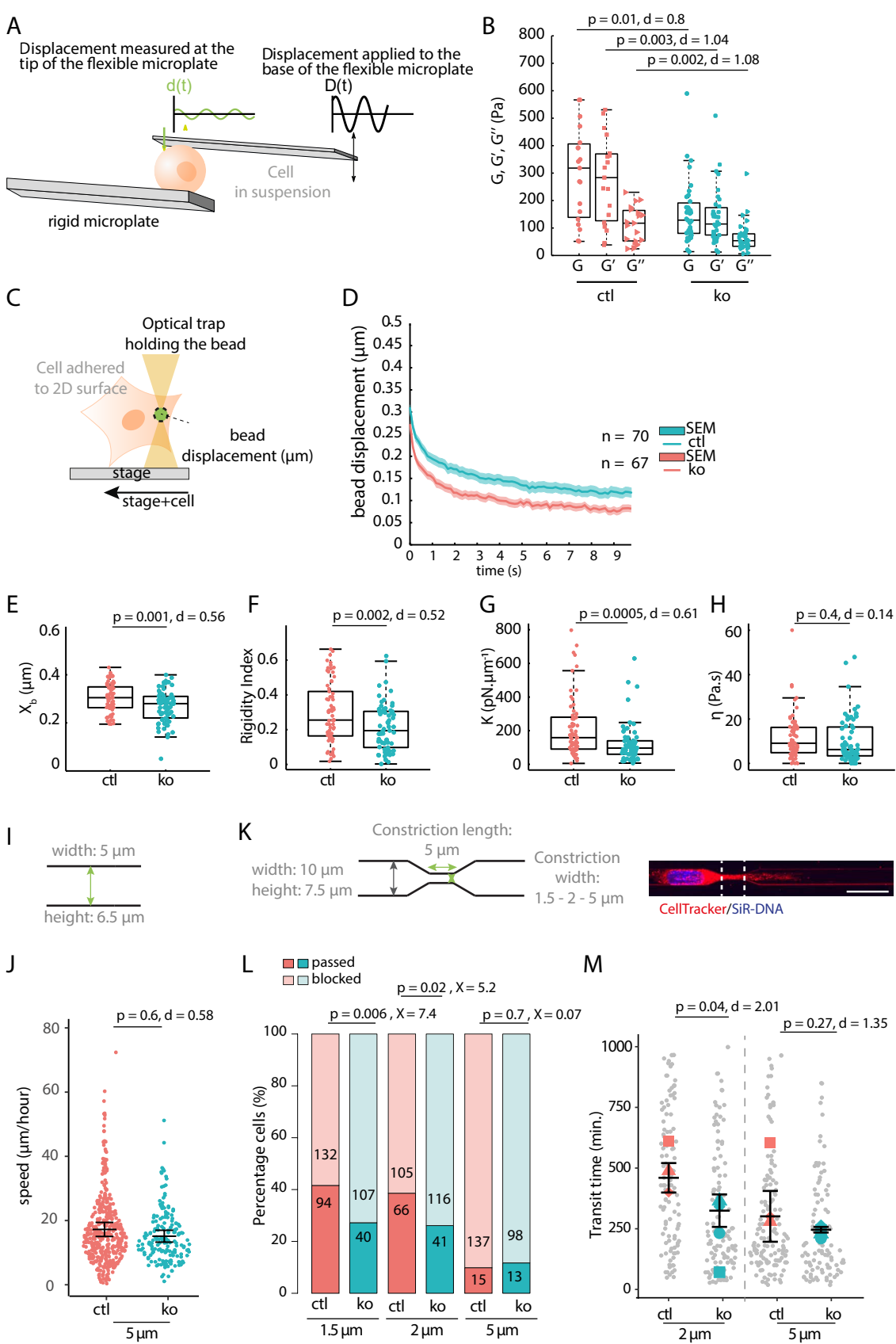


Figure 3

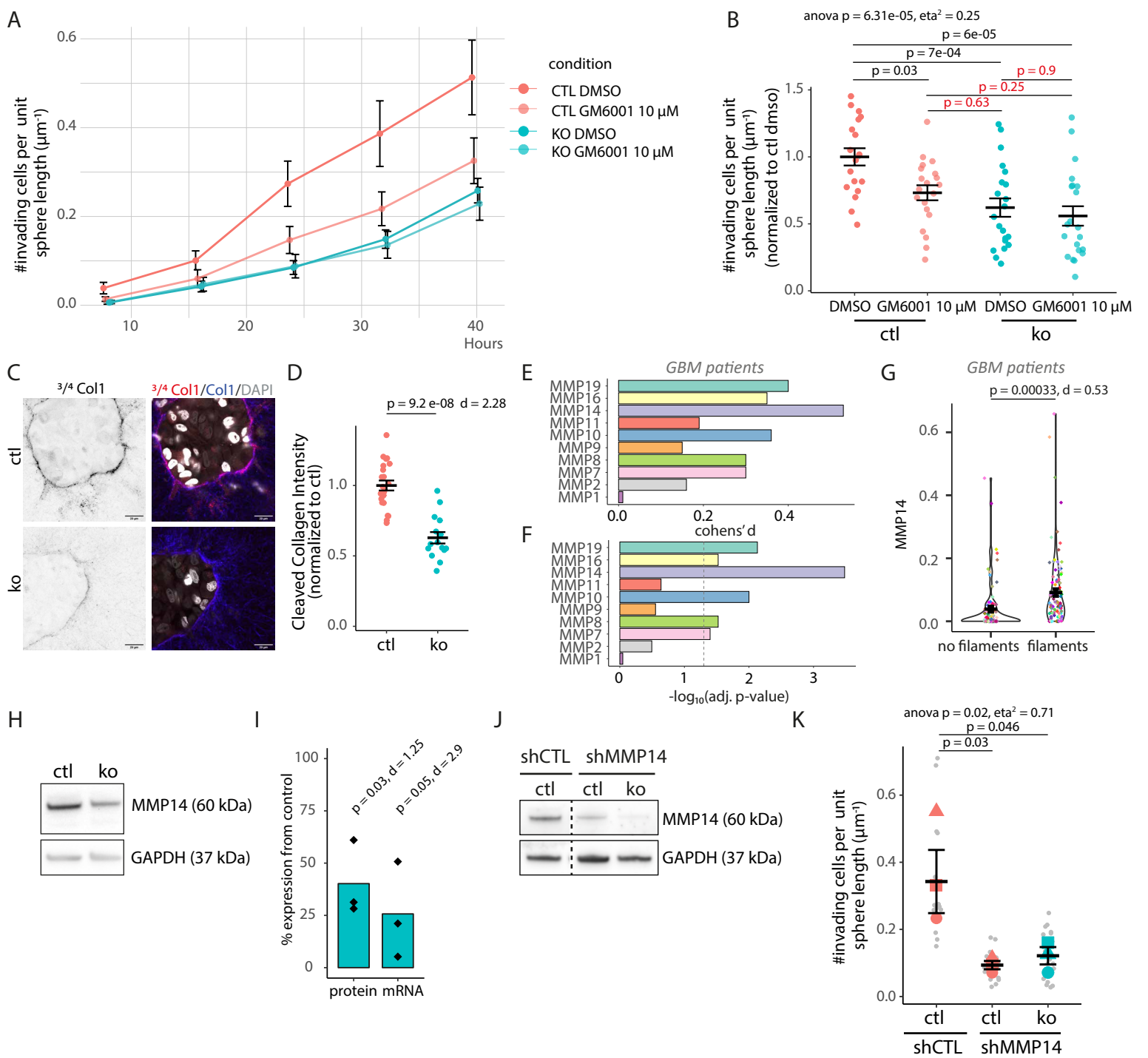
A Schematic of the single cell microplate rheometer. **B** Amplitude of the complex shear modulus (G), storage modulus (G') and loss modulus (G'') measured by the single cell rheometer at frequency $\omega = 0.8$ Hz of ctl ($n = 19$) and ko ($n = 35$) cells. Data was acquired from $N = 3$ biological replicates. P -values are the result of a two-tailed unpaired t -test. **C** Schematic of the optical tweezers-based intracellular microrheometer. **D** Averaged relaxation curves for control (ctl, $n = 70$) and IF-depleted (ko, $n = 67$) cells. **E-H** Phenomenological parameters (bead step amplitude X_b and rigidity index RI) and parameters obtained by fitting the relaxation curves with the standard linear liquid viscoelastic model (spring constant K and viscosity η). Data was acquired from $N = 3$ biological replicates. P -values are the result of a two-tailed unpaired t -test. **I** Geometry of PDMS microchannels. **J** Graph showing the migration speed of cells in $5 \mu\text{m} \times 6.5 \mu\text{m}$ microchannels ($n = 414, 178$). Data was acquired from $N = 3$ biological replicates. P -values are the result of a two-tailed unpaired t -test. **K** Schematic showing the geometry of PDMS microchannels with constrictions and image of a cell migrating through a $1.5 \mu\text{m}$ constriction. *Scale bar = $25 \mu\text{m}$* . **L** Graph showing the percentage cells which passed ('passed') or not ('blocked') through $1.5, 2$ and $5 \mu\text{m}$ -wide constrictions. Absolute number of cells are indicated. P -value and χ^2 show the result of a chi-square test of independence. **M** Transition time of control and ko cells through 2 and $5 \mu\text{m}$ -wide constrictions ($n = 105, 137, 116, 98$). P -values are the result of a two-tailed unpaired t -test on the average transition time for $N = 3$ biological replicates. P values along with Cohen's d effect size coefficients are given on the graphs. Error bars represent SEM.



van Bodegraven et al.
Figure 3

Figure 4

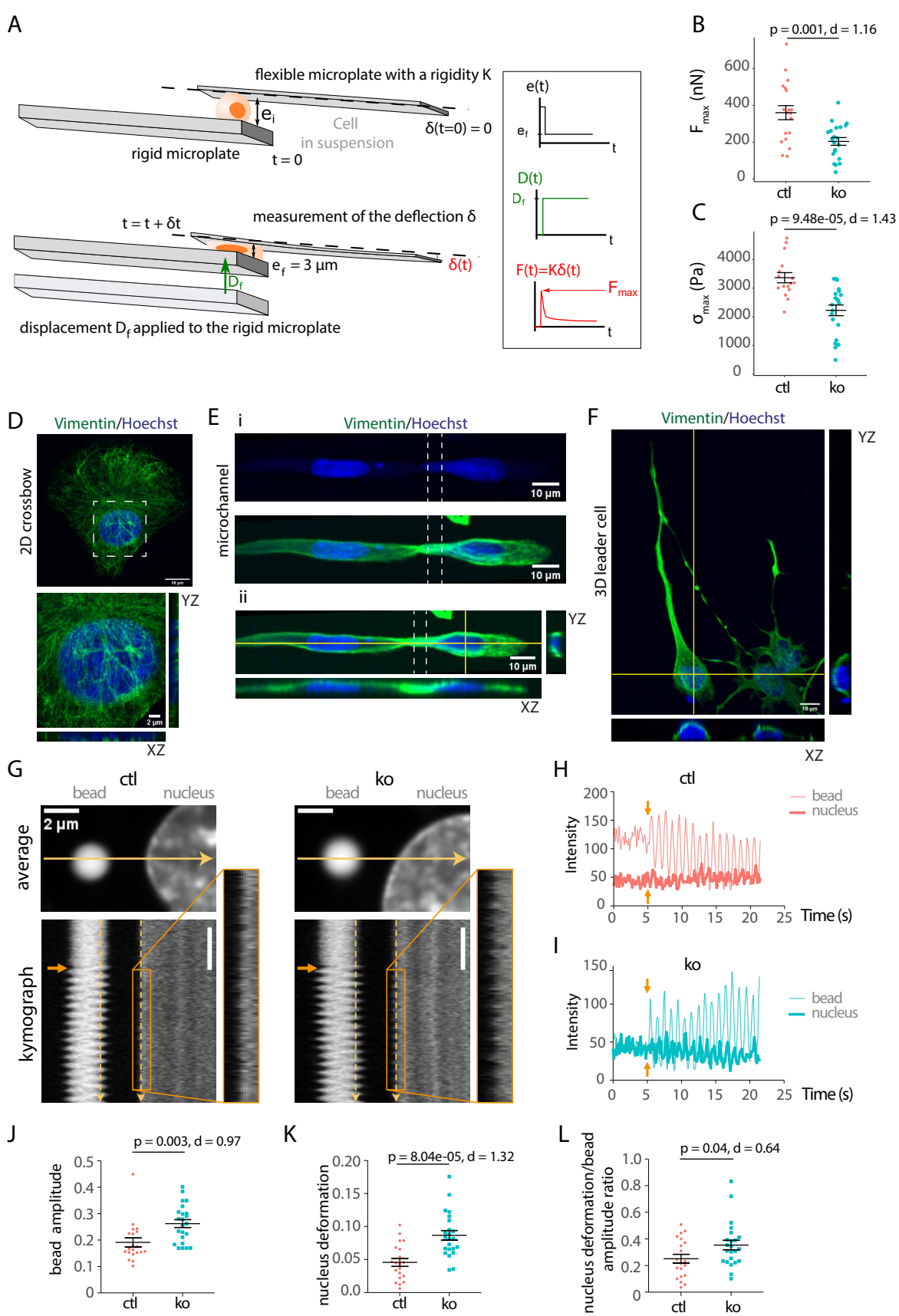
A Quantification of invading cells (normalized by the radius of the sphere at the start of invasion, number of invading cells per unit sphere length (μm^{-1})) as a function of time. During the experiment cells were treated with the metalloproteinase inhibitor GM6001 (10 μM) or DMSO. Error bars (SEM) and data point x-axis positions were adjusted (dodged) to allow visibility of individual error bars and data points. **B** Graph showing the number of invading cells (normalized by the radius of the sphere) after 40 hours of invasion in Matrigel in the indicated treatment conditions ($n = 19, 20, 21, 21$ spheroids). Number of invading cells per unit sphere length (μm^{-1}) values for each spheroid are normalized to the average value of untreated DMSO control spheroids for each biological replicate. The data was acquired from four biologically independent experiments and analysed using a one-way ANOVA followed by a Tukey's HSD post-hoc test. **C** Cleaved collagen ($^3/4\text{Col1}$, red) and collagen 1 (Col1, blue) immunostaining in control (ctl) and IF-depleted (ko) cells invading a 3D collagen matrix. Nuclei are labelled using DAPI (grey). *Scale bar = 20 μm .* **D** Graph showing the cleaved collagen fluorescence intensity for each spheroid normalized by the average cleaved collagen intensity of the control spheroids for each biological replicate ($n = 22, 15$). Data was acquired from $N = 3$ biological replicates. P-values are the result of a two-tailed unpaired t -test. **E, F** Results of two-sided t -tests on patient averages for all expressed MMPs in the patient data in cells with a 'no filaments' or 'filaments' IF signature as determined in Figure 1. **G** Violin plot for MMP14 in cells with a 'no filaments' or 'filaments' IF signature. Diamonds represent the average expression per patient (see Supplementary Figure 3A for patient legend). Two-sided t -tests were realised on patient averages ($N = 99$) and the Cohen's d effect size coefficient is given. **H** Western blot showing MMP14 protein levels in control (ctl) IF-depleted (ko) cells. **I** Quantification of MMP14 protein normalized to GAPDH (westernblot) and MMP14 mRNA (quantitative real-time PCR analysis) normalized by reference genes *GAPDH* and *Aju-J*. Bars represent the average percentage of protein or mRNA expression in IF-depleted (ko) cells compared to control cells and black diamonds represent each individual data point. P-values are the result of a two-sided paired t -test on the normalized protein ($N = 4$) and mRNA expression values ($N = 3$) and Cohen's d effect size coefficients are given. **J** Western blots showing MMP14 and GAPDH protein levels in control (ctl) and IF-depleted (ko) cells stably expressing the indicated shRNA. **K** Graph showing the number of invading cells (normalized by the radius of the sphere) after 40 hours of invasion from shCTL ctl, shMMP14-control and shMMP14-IF-depleted cells. Grey dots represent individual spheroids ($n = 17, 17, 22$). Pink (control spheroids) and blue (IF-depleted spheroids) shapes represent averages of biological replicates. Data was analysed using a one-way ANOVA followed by a Tukey's HSD post-hoc test ($N = 3$). P values along with Cohen's d and eta squared (denoted η^2) effect size coefficients are given on the graphs. Error bars represent SEM.



van Bodegraven et al.
Figure 4

Figure 5

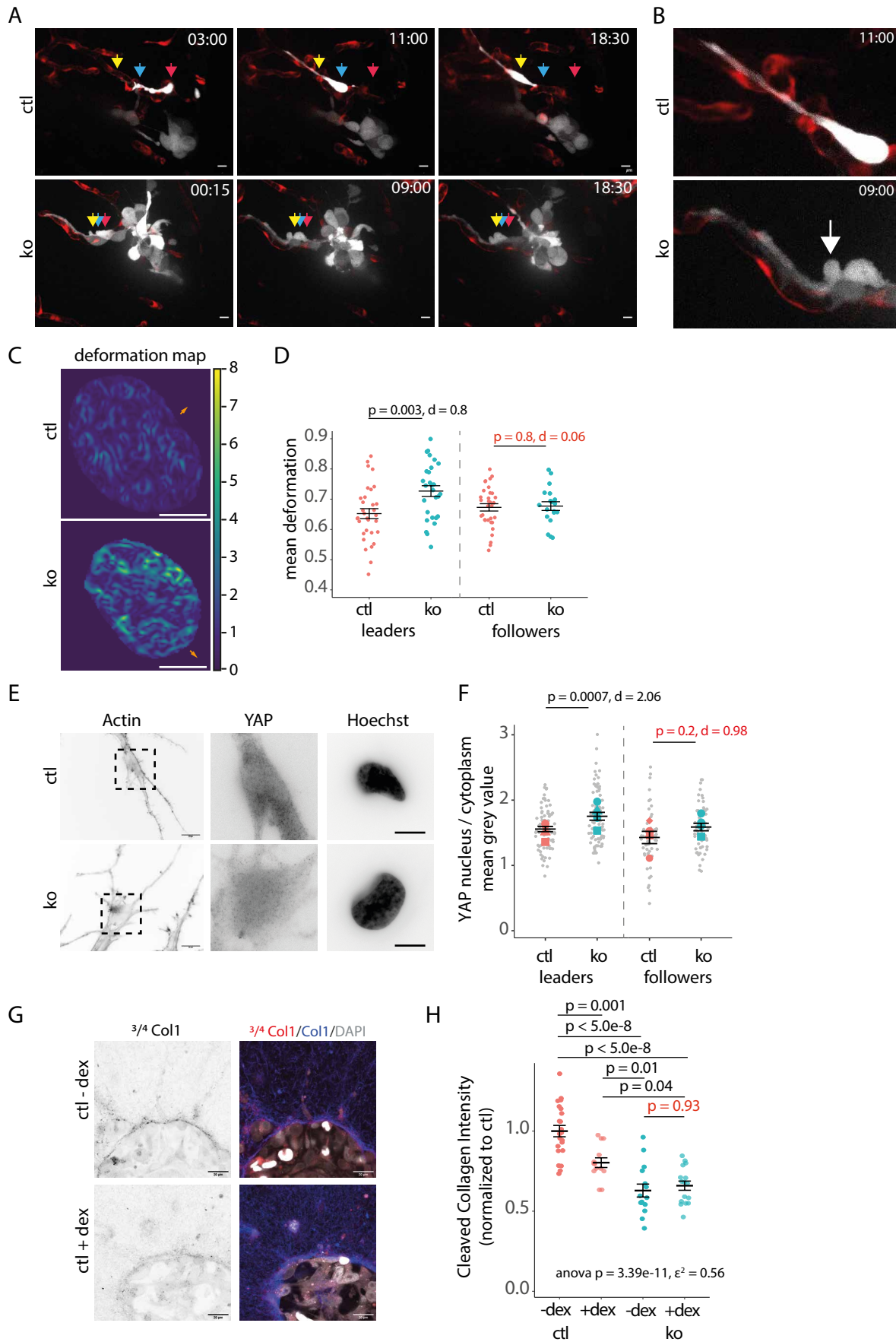
A-C Schematic of the microplate rheology experiment used to deform the cell in suspension from its original size to a 3 μm thickness and measurement of the maximal force (**B**) and stress (**C**) needed for this deformation ($n = 19, 21$ cells). Data was acquired from $N = 3$ biological replicates. P-values are the result of a two-tailed unpaired t -test. **D** Maximum intensity projection of a confocal z-stack of a U251 control cell on a fibronectin-coated crossbow shaped micropattern of $1000 \mu\text{m}^2$ and immunostained for vimentin (green) and labelled with Hoechst (blue). *Scale bar = 10 μm* . **E** (i) Maximum intensity projection of a confocal z-stack of U251 control cell immunostained for vimentin (green) and labelled with Hoechst (blue) passing through a constriction in a microchannel (dotted lines). (ii) Orthogonal views of a confocal z-stack of the nucleus in the constriction. *Scale bar = 10 μm* . **F** Maximum intensity projection and orthogonal views of a confocal z-stack of a U251 control leading cell invading Matrigel immunostained for vimentin (green) and labelled with Hoechst (blue). *Scale bar = 10 μm* . **G** (Top) Average images of typical oscillation experiments in a control (ctl) cell (left) and IF-depleted (ko) cell (right). The bead channel and the nucleus channel were merged. (Bottom) Kymographs along the horizontal yellow lines shown in the average images in the direction of the applied 1Hz oscillations. The green arrows show the time at which the oscillations started. Insets show higher magnification images of the oscillations of the nucleus edge. *Scale bars = 2 μm and 5 sec (kymograph)*. **H, I** Intensity profiles along the dotted yellow lines shown in **G** for the control cell (ctl, top) and the IF-depleted cell (ko, bottom) (thin line: oscillations of the bead, thick line: oscillations of the nucleus edge). The orange arrows show the time at which the oscillations started. **J, K, L** Quantification of the bead amplitude (**J**), the nucleus deformation (**K**) and the ratio between the nucleus deformation and the bead amplitude (**L**) in $n = 20$ control cells (ctl, pink) and $n=23$ IF-depleted cells (ko blue). Data was acquired from $N = 3$ biological replicates. P-values are the result of a two-tailed unpaired t -test. Error bars represent SEM.



van Bodegraven et al.
 Figure 5

Figure 6

A Snapshots of live-cell imaging movies (Supplementary Video 4) of ctl and ko cells (grey) invading along labelled blood vessels (red) in the zebrafish brain. The positions of the cell body at the start (pink), half-way (blue) and at the end (yellow) of live cell image acquisition are indicated with arrows. Times are given in hours. *Scale bar = 10 μ m*. **B** Zoom of invading control (ctl) and IF-depleted (ko) cell. The white arrow indicates blebbing of the cell body in IF-depleted cells. **C** Deformation maps of the nucleus of control (ctl) and IF-depleted (ko) leader cell invading Matrigel obtained from the analysis of 5 minute spinning disk confocal z-stack live images. Orange arrows indicates the direction of invasion. *Scale bar = 5 μ m*. **D** Quantification of nuclear deformations in 3D averaged in time and space each leader ($n = 33$, 28 cells) and follower ($n = 34$, 21 cells) nucleus. The data was acquired from three biologically independent experiments and analysed using two-tailed unpaired *t*-tests. **E** YAP immunostaining of leader control (ctl) and IF-depleted (ko) cells in 75% Matrigel. **F** Quantification of nuclear/cytoplasmic mean grey value of YAP immunostaining in invading ctl and ko leader ($n = 79$, 79 cells) and follower cells ($n = 53$, 59) in Matrigel. Grey dots represent individual cells. Pink (control) and blue (IF-depleted) shapes indicate the averages of biological replicates ($N = 6$ and 5, two-tailed unpaired *t*-test). **G** Cleaved collagen (3/4 Col1, grey and red) and collagen 1 (Col1, blue) immunostaining of control cells invading a 3D collagen matrix in the absence (- dex) and presence (+ dex) of dextran which extracts water from the hydrogels and compresses the gels. Nuclei are labelled using DAPI (grey). *Scale bar = 20 μ m*. **H** Cleaved collagen (3/4 Col1) intensities for control (ctl) and IF-depleted (ko) spheroids in absence (- dex) and presence (+ dex) of dextran normalized by the average cleaved collagen intensity of the control without dextran (ctl – dex) spheroids for each biological replicate ($n = 22$, 13, 15, 16). The data was acquired from three biologically independent experiments and analysed using a one-way ANOVA followed by a Tukey's HSD post-hoc test. P-values along with Cohen's *d* and eta squared (denoted η^2) effect size coefficients are given on the graphs. Error bars represent SEM.



van Bodegraven et al.
Figure 6

Supplementary Files

This is a list of supplementary files associated with this preprint. Click to download.

- [SupplementaryTable1.xlsx](#)
- [SupplementaryTable2.xlsx](#)
- [SupplementaryTable3.xlsx](#)
- [SupplementaryTable4.xlsx](#)
- [SupplementaryInformations.pdf](#)
- [vanBodegravenSupplementaryFigures.pdf](#)
- [SupplementaryVideo1.avi](#)
- [SupplementaryVideo2.avi](#)
- [SupplementaryVideo3.avi](#)
- [SupplementaryVideo4.avi](#)
- [SupplementaryVideo5.mp4](#)